Broken Mirrors

The breakdown of the law of reflection in bilayer graphene

R.Q. Engelberts

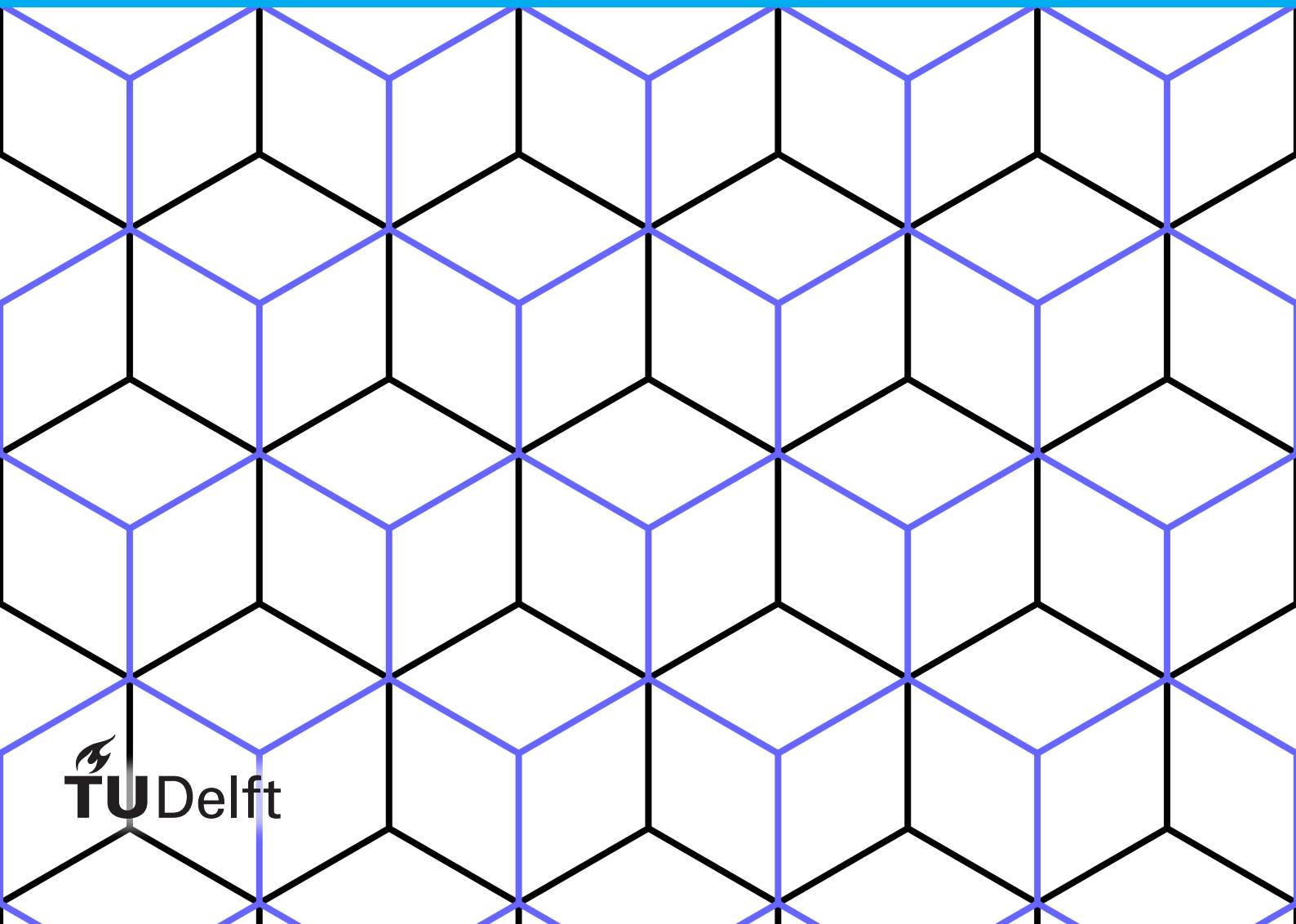

TU Delft

Broken Mirrors

The breakdown of the law of reflection in bilayer graphene

by

R.Q. Engelberts

to obtain the degree of Bachelor of Science
at the Delft University of Technology,
to be defended publicly on Tuesday July 23, 2019 at 1:00 PM.

Student number:	4560752	
Project duration:	September 2018 – July 2019	
Thesis committee:	Dr. A. R. Akhmerov,	TU Delft, supervisor
	Dr. J. L. A. Dubbeldam,	TU Delft, supervisor
	Dr. J. M. Thijssen,	TU Delft
	Dr. G. Carinci,	TU Delft
	Dr. T. O. Rosdahl,	TU Delft
	Dr. K. K. Pöyhönen,	TU Delft

TU Delft

Abstract

As long as a wave has a large enough wavelength, it should reflect off of smooth surfaces specularly: that is what the law of reflection states. This phenomenon is widely known, and used in for instance sonars. Electrons that reflect off of boundaries within conductors should abide this law as well, due to the particle-wave duality. However, it was recently discovered that for disordered graphene boundaries electrons scatter diffusively even when their wavelengths should be long enough not to.

Graphene is a 2-dimensional semiconductor with linear dispersion at low energies, making it a widely researched topic as its applications in future electronic parts are promising. Its bilayer counterpart is made by connecting two layers on top of each other, which in contrast has a quadratic dispersion at low energies. In this work, the specularity of electron reflections within bilayer graphene were studied. This was done by constructing a tight-binding model, where random potentials on the outermost atoms represented imperfections of the lattice. Subsequently the variance of the scattering angle and the scattering phase was analysed, which can be derived using the scattering matrix of the model. This was done numerically for both, and analytically for the phase as well.

It was discovered that the variance of the scattering angle increases cubically with the Fermi wavelength of the electrons. This happens no matter what the distance between the Fermi energy and the disorder mean is, as long as the disorder strength is nonzero. The behaviour of these reflections is the exact opposite of what the law of reflection states. Furthermore, the variance of the scattering phase remains constant when the Fermi energy is close to the disorder mean, and changes inversely proportional to the boundary periodicity if the Fermi energy is further away. Consequently, the variance of the scattering phase versus the Fermi wavelength and the variance of the scattering phase versus the boundary periodicity do not share the same trend in bilayer graphene. More research is needed to verify this phenomenon, which could be done using the continuum description or a magnetic focusing device.

Contents

1 Introduction

A mirror reflects light specularly, which means that the angles of the incident lightbeams relative to the surface equal the reflected ones. This goes against a mechanical way of thinking, as the mirror isn't perfectly flat on a microscopic level. It is the wave-like behaviour of light that causes this phenomenon, known as the *law of reflection*. The mirror should be 'flat' enough for the photons, i.e. its imperfections ought to be smaller than the wavelength of the light. This behaviour has not only been observed for light, but for other forms of waves as well. In sound waves the same effect occurs, which is used for technologies like medical ultrasound. Additionally, surface waves of water or other not-so-viscous fluids behave in the same manner.

The way this phenomenon occurs within conductors, is due to the flow of electrons through these materials. Just like light, electrons have a so-called *particle-wave duality* in their behaviour [1]. What this concept means, is that every particle and wave can be described in terms of each other. In this case, electrons are particles which sometimes behave like waves. One of the key differences between electrons and light, however, is that electrons have mass and charge, while the quanta of light, photons, don't. Nevertheless, because of this concept of duality, it is expected of electrons to follow the law of reflection when reflected off of a boundary within a material. And indeed, most materials seem to abide this law.

It was recently discovered, however, that in a material called *graphene* the law of reflection breaks down[2]. Graphene is a 2D crystalline solid composed of carbon atoms in a honeycomb lattice. Once an electron hits an edge of this 2D material, it gets scattered back into the bulk. However, these edges are not ideal mirrors, due to imperfect lattice termination or hydrogen passivation of dangling bonds [3, 4]. One expects these electrons to follow the law of reflection and bounce back specularly, given that their wavelength is big in comparison to the edge roughness. But due to the linear dispersion of graphene around its K-valleys and the presence of edge bands, this does not always happen.

The intent of this work was to generalise this peculiar phenomenon, by analysing a material called *bilayer graphene*, and studying whether or not this happens more frequently. Graphene itself is interesting, because it is a 2-dimensional semiconductor. That means that it has a thickness on the atomic scale, as opposed to most semiconductors which are multiple atoms thick. These materials are a widely researched topic, due to their great potential in future electric components [5]. It also has a lack of bandgaps at the Dirac points, and a perfectly linear dispersion around those points. By stacking two layers of graphene on top of each other such that one of the layers is shifted along exactly one edge of the hexagons, bilayer graphene is created. This material shares the property of vanishing bandgaps, but actually has a quadratic dispersion around its Dirac points. It also has four distinct bands instead of two, which are also parabolas slightly above and below the K-points.

The second chapter of this thesis describes the uniqueness of graphene and its bilayer counterpart. It also shows their dispersion relation and density of states, and how to derive those. The manners in which the scattering angle and scattering phase are both derived and computed are eludicated in chapter three. After that, the newly found results of this work are listed and discussed in chapter 4, followed by concluding remarks which are presented in chapter 5.

2

Theory

2.1. Graphene and bilayer graphene lattices

As stated in the introduction, graphene is a 2D crystal of carbon atoms arranged in a honeycomb shape. It consists of two nonidentical atoms, which are commonly labelled as A and B. In figure 2.1 these can be seen, along with a green rhombus which is is the unit cell. Repeatedly placing these cells along the vectors a_1 and a_2 results in an infinitely large honeycomb lattice sheet.

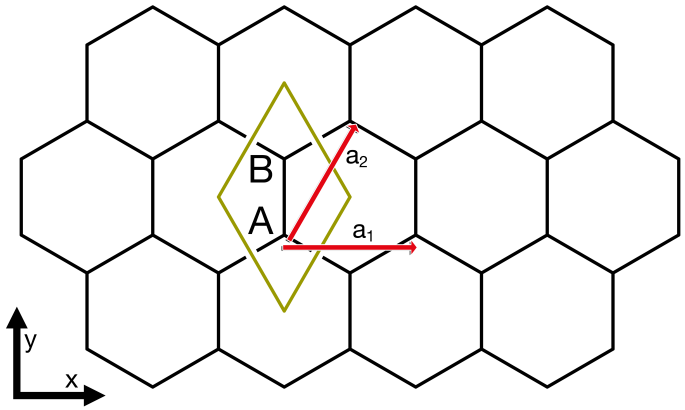

Figure 2.1: Schematic depiction of a small sheet of graphene, where the black lines denote the lattice, and at each of its vertexes a carbon atom is located. The red lines are the Bravais lattice vectors a_1 and a_2, and the green rhombus is the conventional unit cell. Figure made using MarvinSketch [6]

One can take the following definitions of the atom coordinates and the Bravais lattice vectors, where the so-called lattice constant is $a = 2.46$Å[7]. It is important to realise that this length does not equal the carbon-carbon bond length, which is $a/\sqrt{3}$.

$$\mathbf{A} = \left(0,0\right), \quad \mathbf{B} = \left(0, \frac{a}{\sqrt{3}}\right) \tag{2.1}$$

$$\mathbf{a}_1 = \left(a,0\right), \quad \mathbf{a}_2 = \left(\frac{a}{2}, \frac{a\sqrt{3}}{2}\right) \tag{2.2}$$

The edge which results in some strange reflections is the so-called *zigzag edge* of graphene, which can be seen at the bottom and top side of figure 2.1. One can imagine that another edge formation is also possible in graphene, which is called the *armchair edge*. The boundary conditions of a zigzag edge are found in graphene as long as the boundary is not parallel to the carbon-carbon bonds [8]. The reciprocal lattice of graphene is also a hexagon, with again two nonequivalent lattice points. These points are called the K-points, denoted as K and K', and can be seen in figure 2.2:

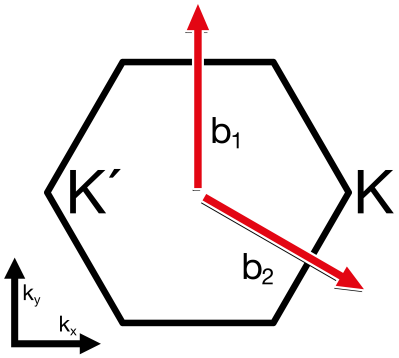

Figure 2.2: Reciprocal lattice of both graphene and bilayer graphene. The hexagon drawn here does not indicate atoms or bonds, but the first Brillouin zone. The non identical reciprocal lattice point K and K' are labelled, and the reciprocal lattice vectors b_1 and b_2 are shown as well. Note that those vectors here only show the direction, not the magnitude. Figure made using MarvinSketch [6]

The sizes and directions of the reciprocal lattice vectors and the locations of the K-points follow from their definition, and are in the chosen representation given as:

$$\mathbf{K} = (\frac{2\pi}{3a}, 0), \quad \mathbf{K}' = (-\frac{2\pi}{3a}, 0) \tag{2.3}$$

$$\mathbf{b}_1 = \left(0, \frac{4\pi}{\sqrt{3}a}\right), \quad \mathbf{b}_2 = \left(\frac{2\pi}{a}, -\frac{2\pi}{\sqrt{3}a}\right) \tag{2.4}$$

Note that the coordinates used for these vectors are in the directions of k_x and k_y, not x and y which are used for the atom coordinates and the Bravais lattice vectors. It is easy to see that for the Bravais lattice vectors and the reciprocal vectors it holds that $a_1 \cdot b_1 = 0$, $a_2 \cdot b_2 = 0$, and $a_1 \cdot b_2 = a_2 \cdot b_1 = 2\pi$.

The lattice of bilayer graphene is very similar to that of graphene. Have in mind that when bilayer graphene is mentioned in this work, it refers to AB-stacked bilayer graphene. That means that above every A-atom in one layer one can find a B-atom of the other. The B-atoms on the first mentioned layer however do not have atoms above or below them, but are in the center of the hexagons of the other layer. This is visualised in figure 2.3b.

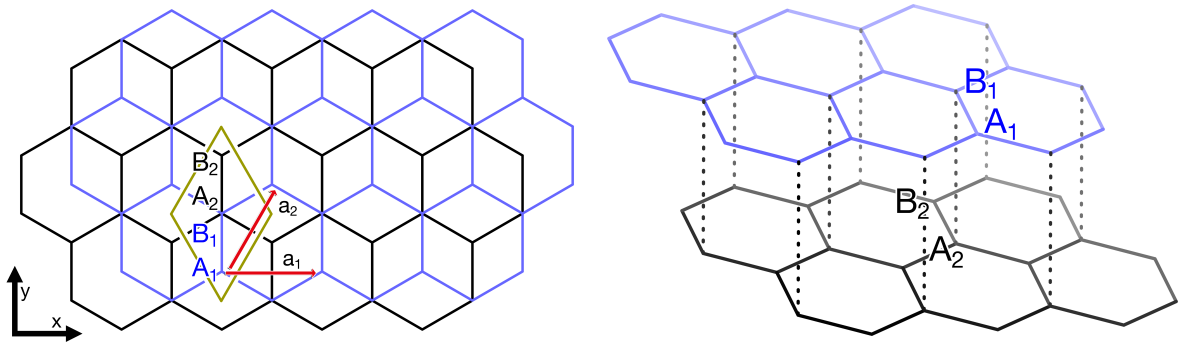

(a) (b)

Figure 2.3: (a) Schematic representation of a small piece of AB-stacked bilayer graphene, where one of the layers is black and the other is blue. Again, the lines indicate the lattice, and the vertexes the atom sites. The four non-identical atoms are labelled A1, B1, A2 and B2, and the green rhombus once again represents the unit cell. At the vertexes where the black and blue lattice cross, both an A2 and a B1 atom are located underneath each other. The red Bravais lattice vectors a_1 and a_2 have the same direction and magnitude as in graphene. (b) 3D representation of a small piece of AB-stacked bilayer graphene. The dotted lines indicate the connections between the two layers. Note that the distances between the layers here are not indicative for the real distance. Figures made using MarvinSketch [6].

The dotted lines in figure 2.3b are the *interlayer hoppings*, as opposed to the *intralayer hoppings*. These connect the two graphene sheets together. In this labelling, it connects the A2-atoms to the B1-atoms. In reality, more next-nearest-neighbour interlayer hoppings are possible [7]. For example, electrons should be able to hop from any atom B1 to one of the three B2's below it. These hoppings are all omitted from this work,

as they increase computation time and do not contribute significantly to the interesting electronic properties. The zigzag edges are studied for bilayer graphene as well, though they are not as straightforward as in monolayer graphene. The one used in the remainder of this project can be seen in the top and bottom of figure 2.3a.

Something else that can be seen is that atom with label A only connect to atoms with label B, in both the graphene sheet and the bilayer graphene sheet. That means that the atoms can be split into two sublattices which only connect with members of the other group. This ensures that both materials have a certain condensed matter property called *chiral symmetry* [9]. That means that there is an operator $\mathscr{C}$ such that for every eigenstate $|\psi\rangle$ of a Hamiltonian H with energy E, there is another eigenstate $\mathscr{C}|\psi\rangle$ with energy $-E$. Moreover, this operator is unitary and squares to +1. The omitted next-nearest-neighbour hoppings actually break this symmetry, so it is an approximate symmetry. Again, the expectation is that their contribution to the observed reflections are minimal and thus these simplifications are made.

Furthermore, both systems follow *time-reversal symmetry* as well. This is a common property, as it basically means the conservation of entropy. Entropy stays constant or increases, the second of which only happens with disturbances to the system. As the graphene and bilayer graphene systems do not per example have an intrinsic magnetic field, this symmetry holds. The third condensed matter symmetry is *particle-hole symmetry*, which is implied to be followed as the other two symmetries are abided by these systems. This symmetry ensures the same negative energy property as the chiral symmetry, except its operator $\mathscr{P}$ is now anti-unitary and can square to either of ± 1. These symmetries are important later on, when the systems are made in numeric simulations. Now that the lattices have been formally introduced among with some properties, a certain property that all waves have can be looked at: the *dispersion relation*.

2.2. Dispersion relation

The dispersion relation of a material is the relation between the energy of its electrons and their momenta. As graphene and its bilayer counterpart are almost infinitesimally thin, only the two momenta parallel to the surface need to be looked at. Both materials can therefore be considered as two-dimensional materials, and the two momenta will be called k_x and k_y as in figure 2.2 . First the *bulk dispersion* of the two materials will be looked at, which is the dispersion relation for a system which extends towards infinity in all its directions. In this case, it should extend infinitely in the $x-$ and y-directions as introduced in figure 2.1. On the vertexes of the hexagonal Brillouin zone in reciprocal space, cones with a linear dispersion are found in graphene. In bilayer graphene, the dispersion around these points are actually parabolic in nature.

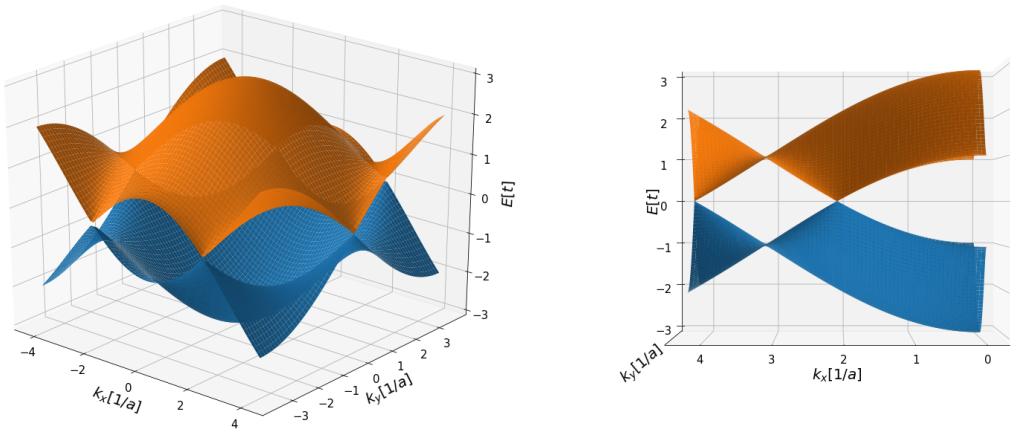

(a) (b)

Figure 2.4: (a): One Brillouin zone of the dispersion relation of an infinite plane of graphene, the so-called bulk dispersion. The labels k_x and k_y indicate the two momenta along the surface, which are perpendicular to each other. The two different coloured bands are degenerate. (b): Side view of a part of the Brillouin zone, to show the linear dispersion around the K-points. Figures made using Kwant [10].

Both figure 2.4 and figure 2.5 were made using Kwant [10], a python package for quantum transport simu-

lations. Once a system is defined, the program can easily solve the Schrödinger equation $H\psi_k = E\psi_k$ to find the allowed energies, where H is the tight binding Hamiltonian and ψ_k a wavefunction with a certain momentum k. The way Kwant constructs the Hamiltonian and how it solves the problem is explained in detail in chapter 3. One can see in figure 2.4 that there are two different bands in graphene. These are of course the valence band (lower) and the conductance band (upper). Furthermore, they are indeed linear around the K-points, following the well known dispersion relation [7]:

$$E_F = \hbar v_F |\mathbf{k}_F| \tag{2.5}$$

The subscript F here denotes that they are actually the Fermi energy, Fermi velocity and Fermi momentum. The value of the Fermi velocity is around $v_F = 10^6 ms^{-1}$. It is also important to not that there is no gap between the two bands, making graphene a gapless semiconductor.

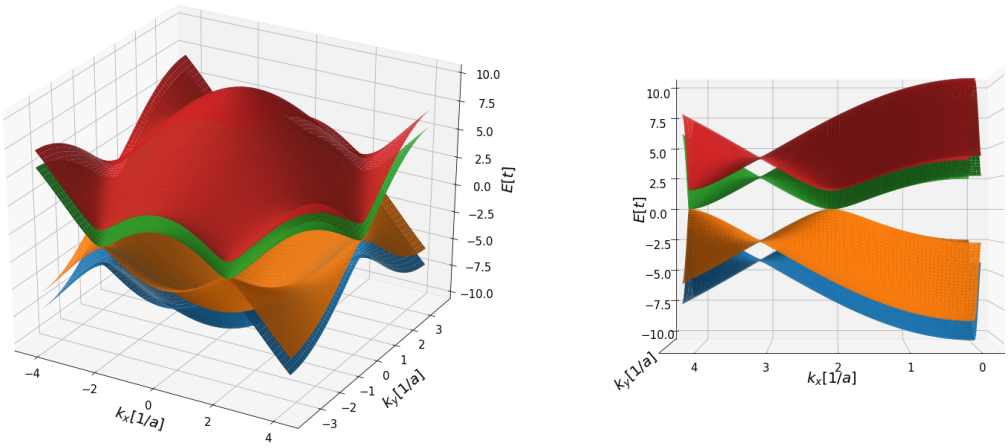

(a) (b)

Figure 2.5: (a): One Brillouin zone of the dispersion relation of an infinite plane of bilayer graphene. The labels k_x and k_y indicate the two momenta along the surface, which are perpendicular to each other. The four different coloured bands are again degenerate states. The hopping parameter γ_1 has been set to $1.5t$ here, to signify the existance of the four bands. It influences the hight of the highest and lowest parabolas, and it decreases the slope slightly. (b): Side view of a part of the Brillouin zone to show the quadratic dispersion around the K-points. Figures made using Kwant [10].

In bilayer graphene, there are actually four bands, which can be seen looking closely at figure 2.5. The closer one gets to the K-points, the more the dispersion resembles two parabolas facing upward, and two parabolas facing downward. A little further away, the dispersion becomes linear as well. The upper two bands are again the conducting bands, and the lower two the valence bands. The lack of gaps between the parabolas make bilayer graphene a gapless semiconductor as well. The slope of these parabolas is known, and can be derived from the following relations [7]:

$$\begin{aligned} \lambda_F &= \frac{2\pi\bar{h}}{\sqrt{2mE_F}} \\ m &= \frac{\gamma_1}{2v^2} \\ v^2 &= \frac{3\gamma_0^2 a^2}{4\bar{h}^2} \end{aligned} \tag{2.6}$$

Here λ stands for the wavelength of the electrons, which is related to the wavevector $\mathbf{k}$ as $\lambda = 2\pi/|\mathbf{k}|$. The parameters γ_0 and γ_1 are the hopping energies between atoms in the same layer, and atoms in the two different layers respectively. Their values are $\gamma_0 = 3.16t$ and $\gamma_1 = 0.381t$, where t is a unit of energy for inplane hopping between nearest neighbours. Combining these equations give an expression of the dispersion near the bottom of the parabolas:

$$E = \frac{3\pi^2}{\lambda^2 \cdot \frac{\gamma_1}{\gamma_0^2}} = \frac{3|\mathbf{k}_F|^2}{4 \cdot \frac{\gamma_1}{\gamma_0^2}} \tag{2.7}$$

The relation is indeed quadratic, as expected for the parabolic shape. This simplification of the dispersion relation is valid as long as $E < \gamma_1$, and therefore only those energies are considered in this work.

Now it is interesting to compare these bulk dispersions above to the *band structure* of a certain system: an infinite zigzag ribbon. For the coordinates used before, this system extends to infinity in the positive and negative x-direction. This choice of direction results in a zigzag edge on both of its sides. Varying over the momentum parallel to the zigzag edges, the following band structure is found:

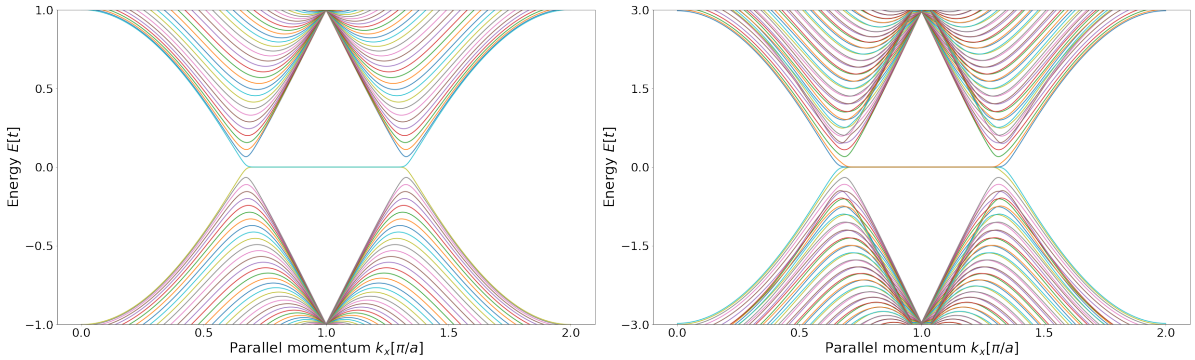

(a) (b)

Figure 2.6: Band structures of infinite zigzag ribbons, where (a) represents one made of graphene and (b) one made of bilayer graphene. Both figures are zoomed in to show the interesting part, which is the flat edge bands. Note that the vertical energy scales of the subfigures are different, as the intralayer hopping parameter was set as t in graphene. The ribbons which were used to generate the bands in this figure are roughly thirty unit cells wide, and were once again made using Kwant [10].

It can be seen here is that there are not only linear and parabolic bands near the K-points, but also flat bands in between. These flat bands connect the two K-points and are a consequence of the choice of zigzag edges. These bands are interesting, as they are not found in many other systems. One example is a so-called *Weyl semimetal* [11]. This is a three dimensional semimetal, which also has parabolic bands at the surface that are connected with flat bands. An example of a system with parabolic bands but no flat edge states is a simple two dimensional square lattice. The existence of these bands in graphene gave rise to an explanation of the breakdown of the law of reflection. This is explained in the next section, using the *density of states* of the system.

2.3. Density of states

The discovery of highly diffusive scattering in graphene systems was unexpected. In order to explain it, the density of states was therefore looked at by Walter et al. As this works aims to generalise the found phenomenon of law-of-reflection-rejecting waves, it has been done here as well for bilayer systems. The density of states in solid state physics describes the amount of states that can be occupied by the system at a certain energy and momentum. The goal of this section is to search for the density of states of modes with no momentum in the direction perpendicular to the boundary. This is called the *local* density of states, in this case at the edge of a semi-infinite sheet of bilayer graphene. The semi-infinite sheet has one infinitely long zigzag edge along the x-direction, and extends infinitely in the positive y-direction. As seen in the previous section about dispersion, a band of states near the edge will then be found called edge states. This band is flat as a function of momentum, and has zero energy, and it connects the two distinct K-points.

Such bands are not found if instead of the zigzag edge, the armchair edge extended infinitely among the x-direction. On that edge, the two valleys are projected onto each other, instead of side by side. This 'dispersion projecting' can be visualised using figure 2.2: calculating it for the zigzag edge projects them in the k_y-direction, and for the armchair edge in the k_x-direction. In figure 2.4b and 2.5b a similar thing is done, using only the first Brillouin zone. In armchair-edged graphene and bilayer graphene, the valleys which are

projected onto each other actually cause birefringence.

There is a distinction that needs to be made for different kinds of momenta to calculate the density of states with. It can be computed using the crystal momentum of the lattice, but also with the kinetic momentum of the electrons. Because the reflections of electrons on the boundary will be studied, the density of states as a function of kinetic momentum is preferred. Normally, the density of states is found by taking the derivative of the amount of states to the energy, $g(E) = \frac{dN}{dE}$. In this case however, the density of states is found by calculating the *Greens function* [12]. With some knowledge of partial differential equations, one should know that this function is the impulse response of a linear operator. That is, for a linear operator D it holds that the Greens function is the solution to the problem $DG(x,x') = \delta(x-x')$, where $\delta(x)$ is *Dirac's delta functional*. Generally, this yields two solutions, one of which is a superposition of outgoing waves and the other a superposition of incoming waves. The solution with incoming waves is called the *advanced Greens function*, and the other the *retarded Greens function*, which are generally defined as:

$$G^R(E) = [E - H + i\eta]^{-1}, \quad G^A = [E - H - i\eta]^{-1} \tag{2.8}$$

Here H is the tight binding Hamiltonian (see chapter 3), and E the energy at which the Greens function is longed to be calculated. The parameter η an infinitesimal positive number which ensures that the wavenumber has a small imaginary part, causing the solutions to be either incoming or outgoing and thus making the Greens function retarded or advanced. In this context, the (retarded) Greens function describes the dynamics of electrons inside conducting materials, while taking leads into account. Leads are infinitely long, like the nano ribbon in the previous section. In the context of semi-infinite sheets, the conducting material is the disordered edge, and the lead the semi-infinite part. Using these two Greens functions, the so-called *spectral function* can be calculated. This function provides information about the nature of the allowed electronic states, regardless whether they are occupied or not. By definition it can actually be considered a generalisation of the local density of states. It is calculated as follows:

$$A \equiv i[G^R - G^A] \tag{2.9}$$

Now, finding the local density of states at a certain energy is easy. By simply dividing the spectral function by 2π it is already found for a certain energy:

$$\rho(E) = \frac{1}{2\pi} A(E) = -\frac{1}{\pi} \mathrm{Im}[G^R(E)] \tag{2.10}$$

The second equality stems from the definition of both Greens functions, as found in equation 2.8. To visualise this quantity, the expectation value is taken of a wave over the local density of states. As the local density of states is already dependent on the energy, a wave is taken with a certain momentum k_x along the boundary. Since only the shape of the density of states is important and not the exact values, the following definition of the local density of states at a certain energy and momentum was chosen:

$$g(E, k_x) = -\mathrm{Im}\big[\, \langle k_x | G(E) | k_x \rangle \,\big] \tag{2.11}$$

The wave is denoted as $|k_x\rangle$ here to signify its dependency on k_x. In the numerical tight-binding calculations, the wave is defined to equal $e^{ik_x x}$ on the edge sites of the semi-infinite zigzag sheet, and zero elsewhere. Note that the angle of the wave actually equals $\mathbf{k}\cdot\mathbf{r}$, where $\mathbf{r}$ is position, as the momentum perpendicular to the boundary k_y is zero. With this knowledge of how to obtain the density of states, infinite systems are now simulated and used to calculate the density of states with.

For the numerical simulations, the Greens function is computed with Kwant by taking the inverse of the Hamiltonian, and then the local density of states by formula 2.11. The Hamiltonian can be derived from the tight binding model which is described in chapter 3. Generating an infinite system isn't doable, as the boundary sites need disorder later on, which would result in infinite inequivalent boundary sites. The Hamiltonian would then also need to become infinitely big, which would make it impossible to numerically invert it. Therefore the edge is made periodic with a certain boundary periodicity parameter L. That means that there are $N = L/a$ distinct unit cells along the boundary, before the system connects to itself again. This can be interpreted as a semi-inifinite cylinder, whose opening consists of a zigzag edge. Given that the parameter L is big enough, this is satisfactory to simulate a semi-infinite sheet. Kwant wraps the system around

by Fourier transforming the Hamitonian in the x-direction, which was the direction that points along the boundary. Clean disorderless systems of graphene and bilayer graphene have a local density of states at their edge as found in figure 2.7.

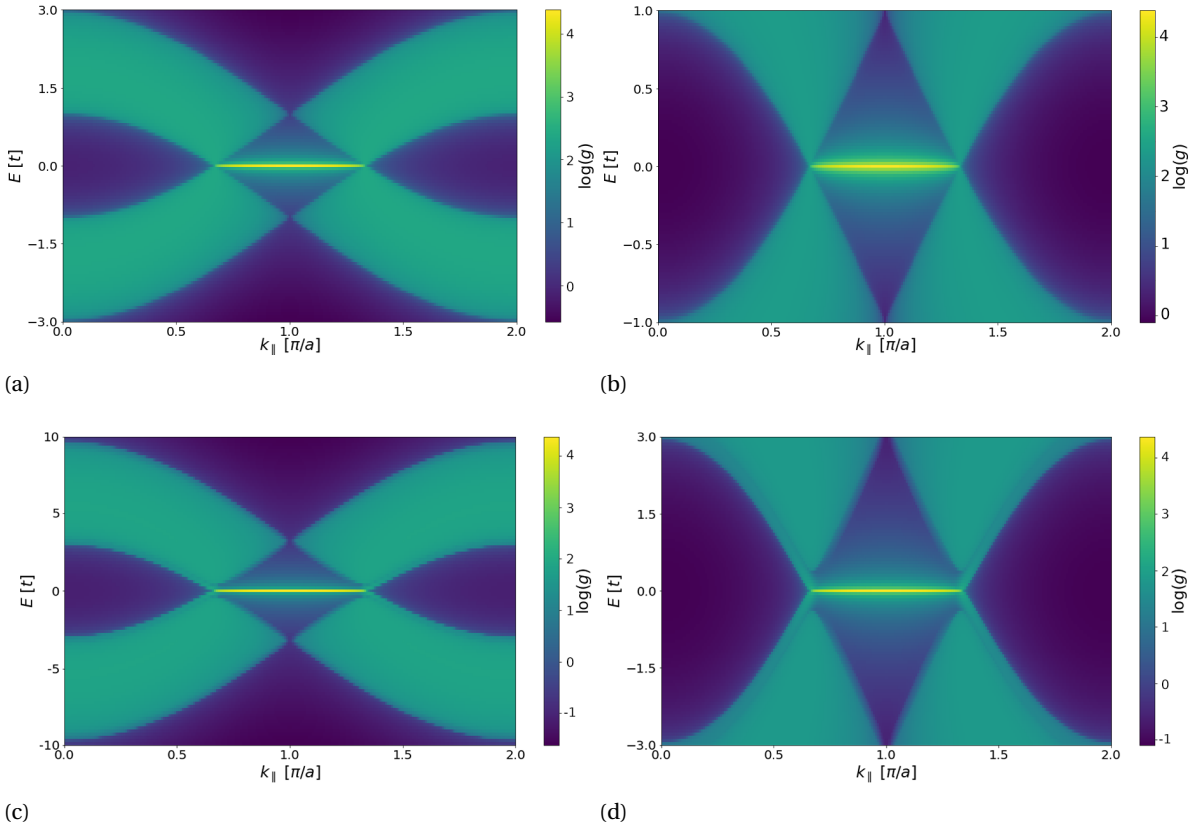

Figure 2.7: Density of states at the edge of semi-infinite sheet with a clean boundary. Figures (a) and (b) show the entire first Brillouin zone of graphene and a smaller portion zoomed in to the two K-valleys. Figures (c) and (d) show the same for bilayer graphene. Both systems used to generate this image had a boundary periodicity of $L = 240a$, and were made using Kwant [10].

Important are the parabolic and linear behaviour around the K-points and the flat edge bands, as mentioned in the previous section about dispersion. One can see that the K-points are indeed located at $k_x = \frac{2}{3}\pi \mod 2\pi$, and $k_x = -\frac{2}{3} \mod 2\pi$, as was found from the reciprocal space.

Interesting behaviour of the density of states is found however when disorder is added onto the edge sites, as it has a strong influence on the edge band. By giving the outermost row of atoms random finite potentials, the density of states changes significantly. These random potentials simulate edge disorder, like hydrogen passivation and dangling bonds. An accurate representation of reality is to have this potential follow a gaussian distribution. If the disorder has a nonzero potential mean V_d, the edge band shifts towards that exact energy. Raising the standard deviation s_d of this disorder potential broadens the band. To visualise the impact of both these paramers, the density of states was calculated for two different scenarios. The first is the density of states when the disorder strength s_d equals zero, the but potential mean V_d doesn't. This certain case is shown in figure 2.8.

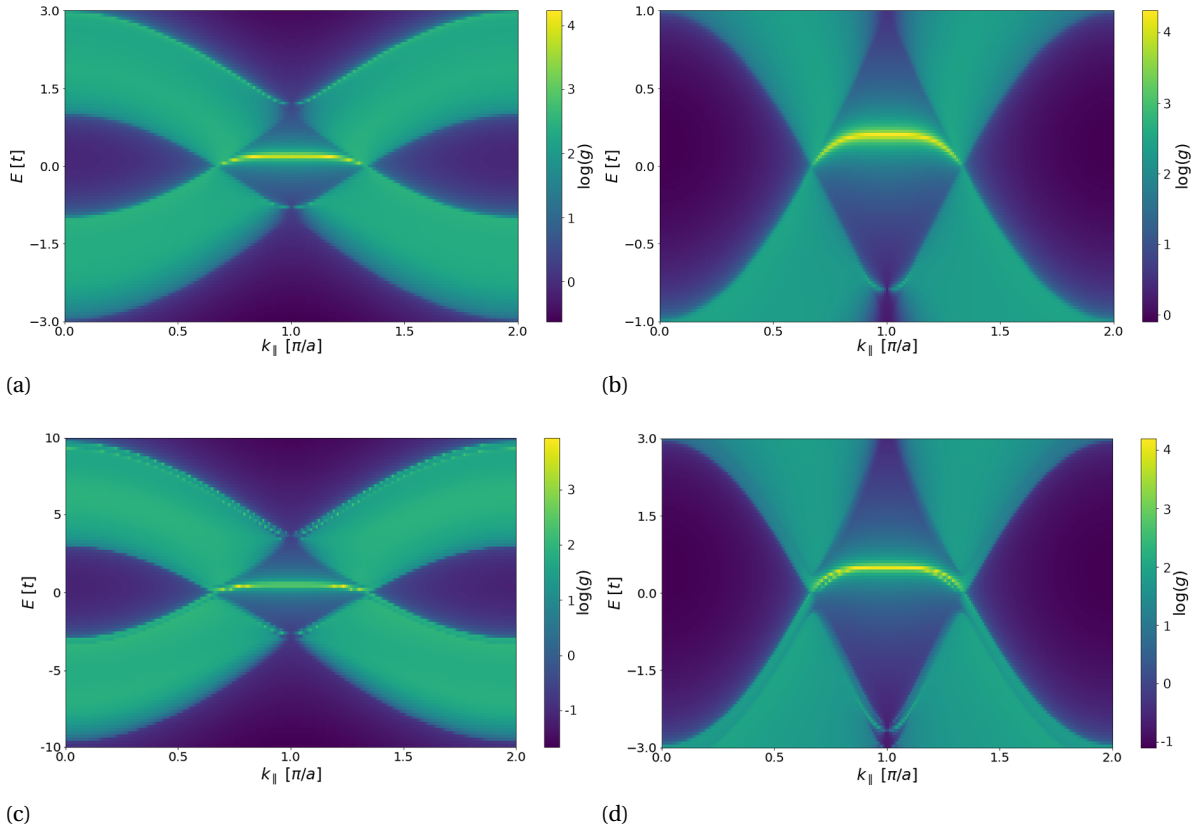

Figure 2.8: Density of states at the edge of a semi-infinite sheet with an offset potential $V_d = 0.2t$ for graphene and $V_d = 0.5t$ for bilayer graphene on the boundary sites. Figures (a) and (b) show the entire first Brillouin zone of graphene and a smaller portion zoomed in to the two K-valleys. Figures (c) and (d) show the same for bilayer graphene. Both systems used to generate this image had a boundary periodicity of $L = 240a$, and were made using Kwant [10].

The flat edge bands have clearly shifted upwards towards the potential V_d. This shifting can contribute to the diffusiveness of the scattering, but is not a direct cause by itself. If all the edge atoms have the exact same onsite energy V_d, they would be identical. Since there is no randomness in the system, and no two states share the same parallel momentum k_x at a certain energy E (given that $E < \gamma_1$), there can be no other state to scatter into but the specular one. Say that the onsite potential of the edge atoms were to go to infinity, they would actually even simulate hard wall boundary conditions.

Randomness only comes into play when the standard deviation of the onsite potentials s_d becomes nonzero, as then all the edge atoms are inequivalent. It can also causes overlap between the edge band and the other bands. In the following figure, the density of states is plotted for a system with both a nonzero mean potential V_d and a nonzero disorder strength s_d:

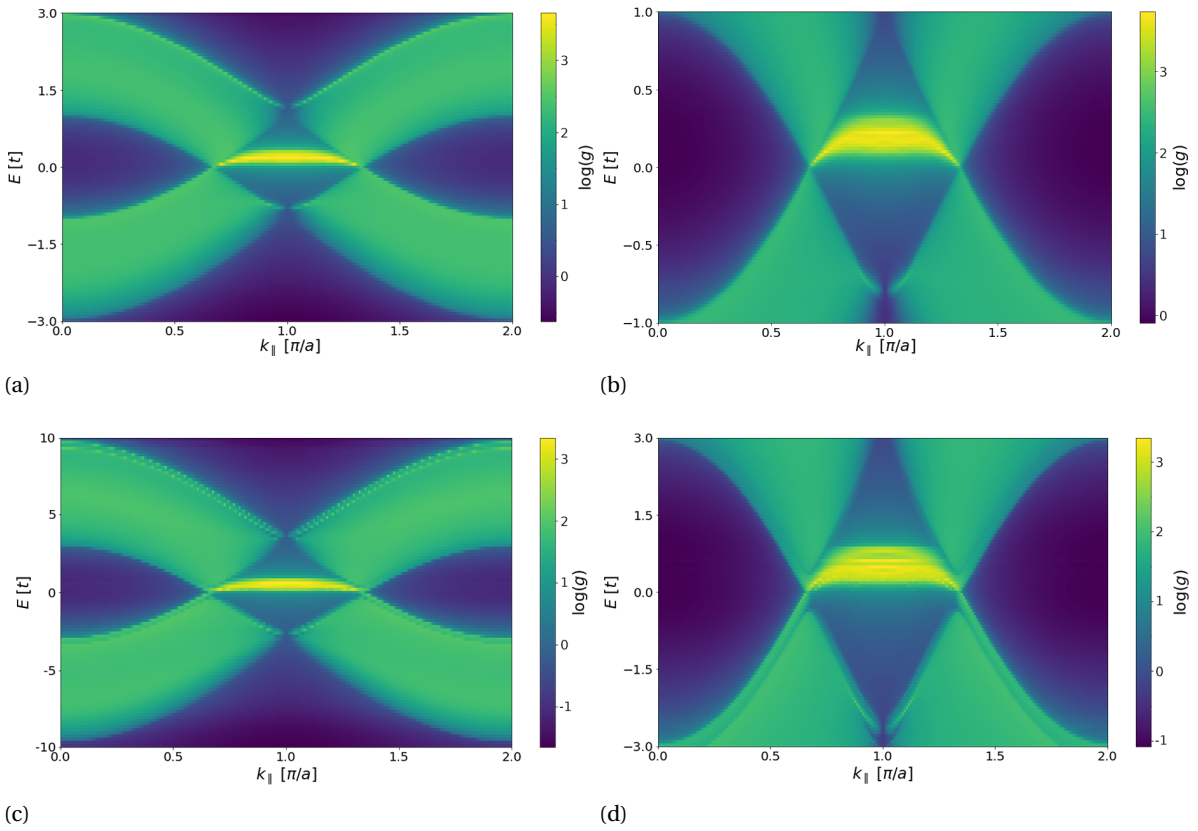

Figure 2.9: Density of states at the edge of a semi-infinite sheets with an offset potential $V_d = 0.2t$ and disorder strength $s_d = 0.1t$ on the boundary sites of graphene, and an offset potential $V_d = 0.5t$ and disorder strength $s_d = 0.3t$ on the boundary sites of bilayer graphene. Figures (a) and (b) show the entire first Brillouin zone of graphene and a smaller portion zoomed in to the two K-valleys. Figures (c) and (d) show the same for bilayer graphene. Both systems used to generate this image had a boundary periodicity of $L = 240a$, and were made using Kwant [10].

Now the edge band has broadened, which was briefly discussed before. All the edge sites have a potential out of a gaussian distribution with a mean of V_d and a standard deviation of s_d, causing randomness along the entire edge. The overlap in energy of the bands is the most clear in figures 2.9b and 2.9d. This was actually found as the requirement for the breakdown of the law of reflection in the paper this work was based on ([2]). If an electron wave possesses a certain energy E_F, then diffusive behaviour is expected when $|E - V_d| \leq s_d$. With the parameters used in figure 2.9, this means that electrons with energies between $0.1t \leq E_F \leq 0.3t$ will scatter diffusively in graphene. This translates into wavelengths between $18a \leq \lambda_F \leq 54a$, using the known linear dispersion relation of graphene: $\lambda_F = \sqrt{3}\pi/E_F$. The rests of this work is dedicated to find if this phenomenon also occurs in bilayer graphene, and to what extent.

Before this chapter ends, a small comparison is made between the local density of states at the zigzag edge and the armchair edge of a semi-infinite bilayer graphene sheet. The density of states at the armchair edge can be seen as the projection in the k_x-direction of the reciprocal space in figure 2.2, and is depicted in figure 2.10.

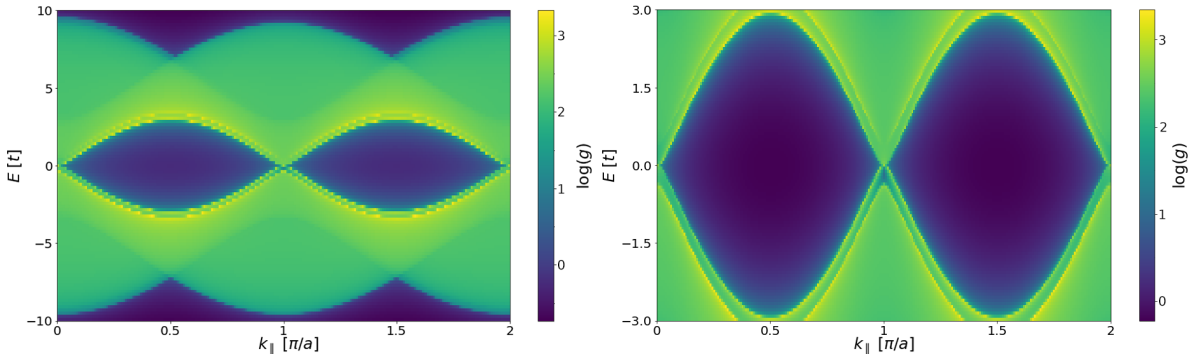

(a) (b)

Figure 2.10: Local density of states at the armchair edge of a semi-infinite bilayer graphene sheet with a clean boundary. Here (a) shows the entire first Brillouin zone, and (b) is zoomed in to the two K-valleys which are projected onto eachother. The system used to make this figure had a periodicity of $L = 240\sqrt{3}a$, because the unit cell is turned sideways. This figure was made using Kwant [10].

No edge states appear in the dispersion relation or the density of states of this system. Due to the projection of the two K-valleys on top of each other, another phenomenon called birefringence occurs at this edge. This is because incoming waves with momentum k_x can always scatter in two different modes with the same parallel momentum. Looking at the density of states, this can be explained by noting that the K-points always overlap, and hence even in disorderless systems the slightly diffusive scattering can happen.

The necessary background information about graphene and its bilayer counterpart which is needed for the rest of this work has now been stated in its entirety. In the next chapter, this knowledge is used to derive ways of describing the specularity of a certain systems' reflections.

3

Method

3.1. Tight binding model

The derivation made in this section is largely the same as appendix B from [2]. It has been discovered that most steps result in the same conclusion or a similar one as in graphene. However, they do not share the same symbolic calculation. Nonetheless, this section is still important for the concluding remarks later on.

The unit cell of bilayer graphene consists of four nonidentical carbon atoms, which were labelled A1, B1, A2 and B2 in the previous chapter. For all derivations in this section, a lattice with orthogonal Bravais lattice vectors is required, and thus a supercell is constructed with 8 atoms.

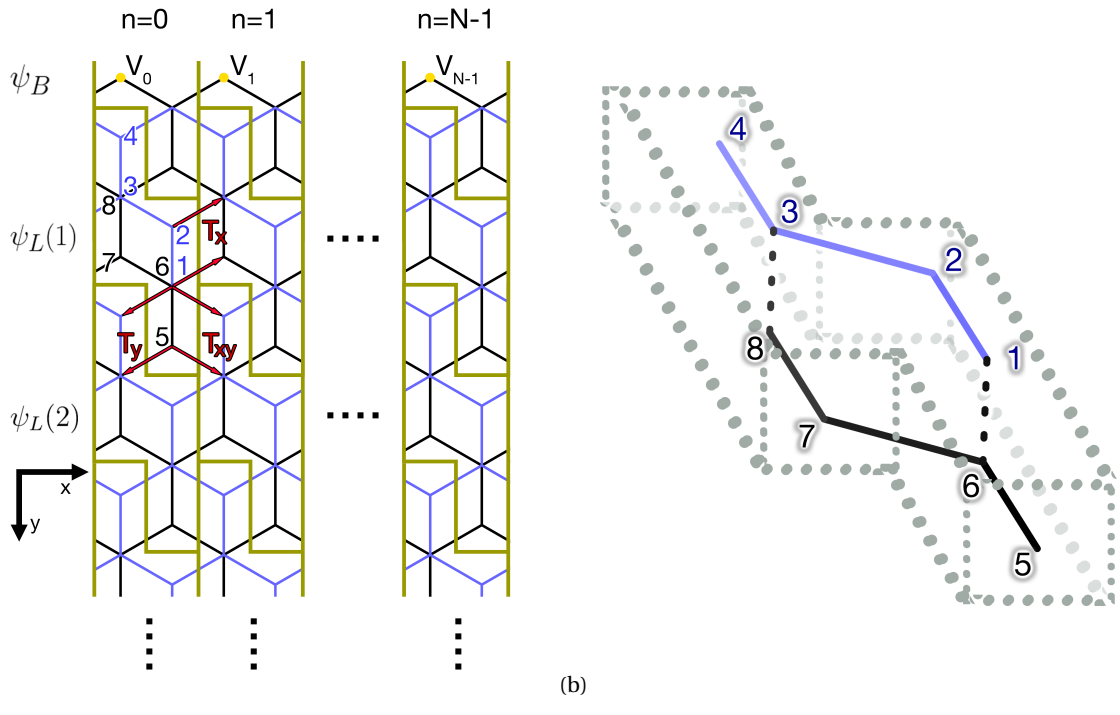

(a) (b)

Figure 3.1: (a) Representation of the tight-binding model of bilayer graphene, using a superlattice with eight atoms sites per unit cell. It is a periodic system with N different sites along the boundary, denoted above, and cell 1 and $N-1$ ar connected all the way around. The notation ψ_B is the boundary unit cell row, and $\psi_L(m)$ the mth lead unit cell row. The numbers 1 to 8 indicate the number each atom is assigned within the supercell. Disorder on the outermost atoms are shown with V_n. (b) A 3D representation of the superlattice unit cell of the semi-infinite zigzag-edged bilayer graphene sheet, where one of the layers is black and the other is blue.

This unit cell is repeated infinitely in the direction away from the boundary, and infinitely along the entire boundary itself. It can be seen that the lattice can actually be made by repeating atoms which are labelled 5, 6,

1 and 2 in figure 3.1b. That would result in the vectors over which the cell is repeated (vectors a_1 and a_2 from equation 2.2) not being orthogonal, and therefore this cell is used. Though this superlattice is normally called a rectangular superlattice, the shape of the cells is not. To be exact, their shape is that of an *S-tetromino*, but the important part is the orthogonality of the translation vectors. These Bravais lattice vectors of the supercell are now defined as:

$$\mathbf{a_1} = (a, 0), \quad \mathbf{a_2} = (0, a\sqrt{3}) \tag{3.1}$$

Here a is the lattice constant as defined in the previous chapter. Within this conventional unit cell, the atoms are given the labels s_1 till s_8 for simplicity. Furthermore, they are described using the following coordinates:

$$\begin{aligned} &\mathbf{s_1} = (\frac{a}{2}, \frac{-a}{2\sqrt{3}}), \quad \mathbf{s_2} = (\frac{a}{2}, \frac{a}{2\sqrt{3}}), \quad \mathbf{s_3} = (0, \frac{a}{\sqrt{3}}), \quad \mathbf{s_4} = (0, \frac{2a}{\sqrt{3}}), \\ &\mathbf{s_5} = (\frac{a}{2}, \frac{-a\sqrt{3}}{2}), \quad \mathbf{s_6} = (\frac{a}{2}, \frac{-a}{2\sqrt{3}}), \quad \mathbf{s_7} = (0, 0), \quad \mathbf{s_8} = (0, \frac{a}{\sqrt{3}}) \end{aligned} \tag{3.2}$$

With this unit cell, a semi-infinite sheet of bilayer graphene is made once again. As seen in figure 3.1a, the system is periodic along the boundary over every N cells. The only difference between these N cells along the boundary will is the random disorder on the outermost carbon atoms V_n, as all other atom sites will have an onsite energy of zero.

In the two layers, the electrons can 'hop' from atom to atom, for which they need a certain energy. This energy is the interlayer hopping energy, which will once again be denoted as γ_0. They can also move between the two layers, as seen in figure 3.1b between atoms s_1 & s_6 and s_3 & s_8. This interlayer hopping potential will similarly be called γ_1 as before.

To continue the tight binding model, a representation of the value of the wavefunction on each individual site is needed. The sites which aren't located on the boundary are called the sites within the lead, or in other words the *lead sites*. As the lead wavefunctions contain 8 sites and the boundary wavefunctions only 4, they must be described in two different ways. The state in the lead is defined as follows:

$$\left|\psi_L\right\rangle = \sum_{m=1}^{\infty} \sum_{n=0}^{N-1} \sum_{j=1}^{8} \psi_L(m,n,j) \left|m,n,j\right\rangle \tag{3.3}$$

Here m describes the y-coordinate of the cell: it is the m'th cell away from the boundary, as seen in figure 3.1a. Note that the direction of y here is flipped in comparison with the previous chapter: now it points away from the boundary, not towards it. As the lead is infinitely long by definition, the parameter m goes from 1 to ∞. The x-coordinate is labelled with n, and since we have periodic boundary conditions there are N different cells in that direction. That means that the entire boundary has a length of $L = Na$. Lastly j denotes which atom within the unit cell is represented, in accordance with figure 3.1b. With that information, $\psi_L(m,n,j) = \left\langle m,n,j\middle|\psi_L\right\rangle$ is the amplitude of the wave function on a certain atom in the corresponding cell. The last term $\left|m,n,j\right\rangle$ is the atomic orbital as usual. The wavefunctions on the boundary are on the other hand given as:

$$\left|\psi_B\right\rangle = \sum_{n=0}^{N-1} \sum_{j\in\{1,5,6,7\}} \psi_B(n,j) \left|0,n,j\right\rangle \tag{3.4}$$

By taking these four atoms as the only sites within the boundary cells, a nice zigzag edge is constructed on both layers. Once again the term $\psi_B(n,j) = \left\langle 0,n,j\middle|\psi_B\right\rangle$ signifies the amplitude on the boundary. The imperfections of the lattice will be simulated by applying a random potential V_n on atoms on site 7 in the boundary cells. This random potential follows a Gaussian distribution, with mean V_d and variance s_d^2 as stated in the previous chapter. Combining all this information results in the following Hamiltonian:

$$H = -\gamma_0 \sum_{<mnj,m'n'j'>} \left|m,n,j\right\rangle\left\langle m',n',j'\right| - \gamma_1 \sum_{<mnj,m^*n^*j^*>} \left|m,n,j\right\rangle\left\langle m^*,n^*,j^*\right| + \sum_n V_n \left|0,n,7\right\rangle\left\langle 0,n,7\right| \tag{3.5}$$

The subscript of the first sum indicates that it is only for sites which are connected in the same layer. The subscript of the second sum makes sure that it only sums when two sites are on top of eachother, as it

describes the interlayer hopping. For a tight-binding hamiltonian, the following wavefunction is constructed to apply it on (in vector form):

$$\psi = \begin{pmatrix} \psi_L \\ \psi_B \end{pmatrix} = \begin{pmatrix} \vdots \\ \psi_L(2) \\ \psi_L(1) \\ \psi_B \end{pmatrix} = \begin{pmatrix} \vdots \\ \psi_L(2,0) \\ \psi_L(1,L-1) \\ \vdots \\ \psi_L(1,0) \\ \psi_B(L-1) \\ \vdots \\ \psi_B(0) \end{pmatrix}, \quad \psi_L(m,n) = \begin{pmatrix} \psi_L(m,n,1) \\ \psi_L(m,n,2) \\ \vdots \\ \psi_L(m,n,8) \end{pmatrix}, \quad \psi_B(n) = \begin{pmatrix} \psi_B(n,1) \\ \psi_B(n,5) \\ \psi_B(n,6) \\ \psi_B(n,7) \end{pmatrix} \tag{3.6}$$

Individual locations of the amplitudes of the components of this wavefunctions can be located in figure 3.1a. The lead wavefunctions $\psi_L(m,n)$ here contain all 8 atom sites individually of the supercells, as a vector. The boundary wavefunctions correspondingly contain the four boundary sites mentioned before, which are ordered numerically: 1, 5, 6, 7. On these length 8 lead wavefunctions, the following matrix operations can be used:

$$H_0 = \begin{bmatrix} 0 & -\gamma_0 & 0 & 0 & 0 & -\gamma_1 & 0 & 0 \\ -\gamma_0 & 0 & -\gamma_0 & 0 & 0 & 0 & 0 & 0 \\ 0 & -\gamma_0 & 0 & -\gamma_0 & 0 & 0 & 0 & -\gamma_1 \\ 0 & 0 & -\gamma_0 & 0 & 0 & 0 & 0 & 0 \\ 0 & 0 & 0 & 0 & 0 & -\gamma_0 & 0 & 0 \\ -\gamma_1 & 0 & 0 & 0 & -\gamma_0 & 0 & -\gamma_0 & 0 \\ 0 & 0 & 0 & 0 & 0 & -\gamma_0 & 0 & -\gamma_0 \\ 0 & 0 & -\gamma_1 & 0 & 0 & 0 & -\gamma_0 & 0 \end{bmatrix}, \quad T_x = \begin{bmatrix} 0 & 0 & 0 & 0 & 0 & 0 & 0 & 0 \\ 0 & 0 & 0 & 0 & 0 & 0 & 0 & 0 \\ 0 & -\gamma_0 & 0 & 0 & 0 & 0 & 0 & 0 \\ 0 & 0 & 0 & 0 & 0 & 0 & 0 & 0 \\ 0 & 0 & 0 & 0 & 0 & 0 & 0 & 0 \\ 0 & 0 & 0 & 0 & 0 & 0 & 0 & 0 \\ 0 & 0 & 0 & 0 & 0 & -\gamma_0 & 0 & 0 \\ 0 & 0 & 0 & 0 & 0 & 0 & 0 & 0 \end{bmatrix},$$
$$T_y = \begin{bmatrix} 0 & 0 & 0 & 0 & 0 & 0 & 0 & 0 \\ 0 & 0 & 0 & 0 & 0 & 0 & 0 & 0 \\ 0 & 0 & 0 & 0 & 0 & 0 & 0 & 0 \\ -\gamma_0 & 0 & 0 & 0 & 0 & 0 & 0 & 0 \\ 0 & 0 & 0 & 0 & 0 & 0 & 0 & 0 \\ 0 & 0 & 0 & 0 & 0 & 0 & 0 & 0 \\ 0 & 0 & 0 & 0 & 0 & 0 & 0 & 0 \\ 0 & 0 & 0 & 0 & -\gamma_0 & 0 & 0 & 0 \end{bmatrix}, \quad T_{xy} = \begin{bmatrix} 0 & 0 & 0 & 0 & 0 & 0 & 0 & 0 \\ 0 & 0 & 0 & 0 & 0 & 0 & 0 & 0 \\ 0 & 0 & 0 & 0 & 0 & 0 & 0 & 0 \\ -\gamma_0 & 0 & 0 & 0 & 0 & 0 & 0 & 0 \\ 0 & 0 & 0 & 0 & 0 & 0 & 0 & 0 \\ 0 & 0 & 0 & 0 & 0 & 0 & 0 & 0 \\ 0 & 0 & 0 & 0 & 0 & 0 & 0 & 0 \\ 0 & 0 & 0 & 0 & -\gamma_0 & 0 & 0 & 0 \end{bmatrix}, \tag{3.7}$$

The matrix H_0 has all the hoppings within a single unit cell itself. The nonzero elements are indeed located on the elements which connect connected atoms: e.g. the element in the first row and the second column having value $-\gamma_0$ means that hopping from site s_1 to s_2 takes that exact energy. In the off-diagonal 4 by 4 blocks, the interlayer hoppings γ_1 are found. The second matrix T_x is the one representing the hoppings between superlattice unit cells in the direction along the boundary x, as seen in figure 3.1a. Likewise T_y shows the hoppings in the direction perpendicular to the boundary y, and T_{xy} the diagonal hoppings. Note that T_y and T_{xy} are actually the same matrix, but describe different movements. There are four more matrices of a similar small size, that describe the movement within the boundary cells and connect the boundary to the lead sites. These are different, as the boundary sites contain just 4 atoms instead of the regular 8:

$$H^B_{0,n} = \begin{bmatrix} 0 & 0 & -\gamma_1 & 0 \\ 0 & 0 & -\gamma_0 & 0 \\ -\gamma_1 & -\gamma_0 & 0 & -\gamma_0 \\ 0 & 0 & -\gamma_0 & V_n \end{bmatrix}, \quad T^B_x = \begin{bmatrix} 0 & 0 & 0 & 0 \\ 0 & 0 & 0 & 0 \\ 0 & 0 & 0 & 0 \\ 0 & 0 & -\gamma_0 & 0 \end{bmatrix},$$
$$T^B_y = \begin{bmatrix} 0 & 0 & 0 & 0 \\ 0 & 0 & 0 & 0 \\ 0 & 0 & 0 & 0 \\ -\gamma_0 & 0 & 0 & 0 \\ 0 & 0 & 0 & 0 \\ 0 & 0 & 0 & 0 \\ 0 & 0 & 0 & 0 \\ 0 & -\gamma_0 & 0 & 0 \end{bmatrix}, \quad T^B_{xy} = \begin{bmatrix} 0 & 0 & 0 & 0 \\ 0 & 0 & 0 & 0 \\ 0 & 0 & 0 & 0 \\ -\gamma_0 & 0 & 0 & 0 \\ 0 & 0 & 0 & 0 \\ 0 & 0 & 0 & 0 \\ 0 & 0 & 0 & 0 \\ 0 & -\gamma_0 & 0 & 0 \end{bmatrix} \tag{3.8}$$

Another difference can be seen in the onsite hamiltonian for the boundary sites $H^B_{o,n}$, as it contains the random onsite potential term V_n on site 7. This is also different from the graphene tight-binding analysis, as there all the boundary cells contain just the site with disorder. These eight matrices work on the small wavefunctions $\psi_L(m,n)$ and $\psi_B(n)$. The complete infinitely sized tight binding hamiltonian that works on the wavefunction ψ as defined in equation 3.6 is then constructed as:

$$H = \begin{bmatrix} \ddots & \ddots & & \\ \ddots & H_L & T_L & \\ & T_L^\dagger & H_L & T_{LB} \\ & & T_{LB}^\dagger & H_B \end{bmatrix} \tag{3.9}$$

In here, four new matrices are introduced again. H_L is a $8L \times 8L$ matrix which describes the movement between two adjacent cells in a single row within the lead. Then, T_L and $T_L^\dagger$ address the movement between two adjacent cells of the infinite amount of cells within a column, and is also $8L \times 8L$. The superscript † here represents the hermitian conjugate Their boundary counterparts once again are denoted with H_B, T_{LB} and $T_{LB}^\dagger$, which are respectively $4L \times 4L$, $8L \times 4L$ and $4L \times 8L$. These matrices are built from the previous smaller ones like this:

$$H_L = \begin{bmatrix} H_0 & T_x & & T_x^\dagger \\ T_x^\dagger & H_0 & \ddots & \\ & \ddots & \ddots & T_x \\ T_x & & T_x^\dagger & H_0 \end{bmatrix}, \quad T_L = \begin{bmatrix} T_y & T_{xy} & & \\ & T_y & \ddots & \\ & & \ddots & T_{xy} \\ T_{xy} & & & T_y \end{bmatrix},$$
$$H_B = \begin{bmatrix} H^B_{0,0} & T^B_x & & T^{B\dagger}_x \\ T^{B\dagger}_x & H^B_{0,1} & \ddots & \\ & \ddots & \ddots & T^B_x \\ T^B_x & & T^{B\dagger}_x & H^B_{0,L-1} \end{bmatrix}, \quad T_{LB} = \begin{bmatrix} T^B_y & T^B_{xy} & & \\ & T^B_y & \ddots & \\ & & \ddots & T^B_{xy} \\ T^B_{xy} & & & T^B_y \end{bmatrix} \tag{3.10}$$

The tight binding model is now complete. From this the scattering matrix can be derived, and from that the scattering phase. What's more important is that the dependencies of the *variance* of the scattering phase can be concluded. With this a conclusion can be made about the specularity of the reflections of electrons at the boundary, which is the goal. To get this scattering matrix, a distinguishment between the possible eigenstates in the lead is necessary. This is done by temporarily neglecting the boundary, such that an infinite translationally invariant system is created. This system has the following Hamiltonian and wavefunction:

$$H^{\text{inf}} = \begin{bmatrix} \ddots & \ddots & & \\ \ddots & H_L & T_L & \\ & T_L^\dagger & H_L & \ddots \\ & & \ddots & \ddots \end{bmatrix}, \quad \psi^{\text{inf}} = \begin{pmatrix} \vdots \\ \psi_L(2) \\ \psi_L(1) \\ \vdots \end{pmatrix} \tag{3.11}$$

For any wavefunction $\psi_L^{\text{inf}}(m)$ over the m'th row in this infinite lead, the Schrödinger equation [13] can now be extracted from equation 3.11:

$$T_L^\dagger \psi_L^{\text{inf}}(m+1) + H_L \psi_L^{\text{inf}}(m) + T_L \psi_L^{\text{inf}}(m-1) = E\psi_L^{\text{inf}}(m) \tag{3.12}$$

Since this equation resides in a periodically-repeating environment, a Bloch Ansatz [14] is used to simplify the problem:

$$\psi_L^{\text{inf}}(m,n) = \lambda^m \xi^n \chi \tag{3.13}$$

The eigenvalue of the translation operators are used here, with λ for the one in the y-direction, and ξ for the one in the x-direction. Then χ gives information about the structure of the wave function within the unit cell, and therefore has eight elements. The periodicity in the direction along the boundary forces the eigenvalue of T_x to be a periodic function as well, as $\xi^N = 1$ must hold. That means that ξ obeys the following:

$$\xi_\nu = e^{ik_{x,\nu}a} = e^{\frac{2\pi i \nu}{N}} \tag{3.14}$$

This means that the values of the x-momentum $k_{x,\nu}$ are then restricted to N different values, being $\frac{2\pi\nu}{aN}$ and it is denoted with the subscript ν which reaches from 0 to $N-1$.

The analysis becomes easier if the Fermi energy is assumed to be zero, as there are only four states possible at that energy. The x-momenta of those modes lie at the exact location of the K-points, where the parabolas meet in the dispersion relation. The coordinates of these points are $K_x = 2\pi/3a$ and $K_x' = -2\pi/3a$, as discussed in the previous chapter. One consequence of this is that the boundary periodicity N must be a multiple of 3ν, due to the just introduced definition of the eigenvalue of the translation operator. Note that this also holds in the numerical analysis done in Kwant later. Using this Bloch ansatz and a zero-energy assumption, equation (3.12) simplifies to:

$$\left[H_0 + (\xi_\nu^{-1} T_x + \lambda^{-1} T_y + \xi_\nu^{-1}\lambda^{-1} T_{xy} + \text{h.c.})\right]\chi = H_c\chi = 0 \tag{3.15}$$

The text "h.c." here stand for hermitian conjugate, which needs to be added of the other terms within the brackets. One thing to note here is that the eigenvalue of the diagonal translation operator T_{xy} is assumed to be $\xi_\nu\lambda$. This is a direct consequence of choosing the superlattice to be rectangular (read: orthogonal Bravais lattice vectors), hence another reason why it was chosen. The matrix H_c in its entirety is:

$$H_c = \begin{bmatrix}
0 & -\gamma_0 & 0 & -\gamma_0\lambda(1+\xi_\nu) & 0 & -\gamma_1 & 0 & 0 \\
-\gamma_0 & 0 & -\gamma_0(1+\xi_\nu) & 0 & 0 & 0 & 0 & 0 \\
0 & -\gamma_0(1+\frac{1}{\xi_\nu}) & 0 & -\gamma_0 & 0 & 0 & 0 & -\gamma_1 \\
\frac{-\gamma_0(1+\frac{1}{\xi_\nu})}{\lambda} & 0 & -\gamma_0 & 0 & 0 & 0 & 0 & 0 \\
0 & 0 & 0 & 0 & 0 & -\gamma_0 & 0 & -\gamma_0\lambda(1+\xi_\nu) \\
-\gamma_1 & 0 & 0 & 0 & -\gamma_0 & 0 & -\gamma_0(1+\xi_\nu) & 0 \\
0 & 0 & 0 & 0 & 0 & -\gamma_0(1+\frac{1}{\xi_\nu}) & 0 & -\gamma_0 \\
0 & 0 & -\gamma_1 & 0 & \frac{-\gamma_0(1+\frac{1}{\xi_\nu})}{\lambda} & 0 & -\gamma_0 & 0
\end{bmatrix} \tag{3.16}$$

The relation between the two translational eigenvalues is needed, to find the requirement for H_C to have eigenvalue zero, i.e. the zero energy assumption. This can easily be done by checking when the determinant of this matrix equals zero, so solving $\det(H_c) = 0$ and rewriting that expression to λ as a function of ξ_ν. Note that then the eigenvalue λ is also dependent on ν, and therefore it will receive the same subscript. The determinant problem has been solved analytically using Mathematica [15], and resulted in the following two possible relations:

$$\lambda_v^+ = \frac{(1+\xi_v)^2}{\xi_v}, \quad \lambda_v^- = \frac{\xi_v}{(1+\xi_v)^2} \tag{3.17}$$

These are the exact same relations as found in monolayer graphene. That can easily be explained by looking at the difference between the matrices H_C in bilayer graphene and in two decoupled monolayer graphene systems. The only difference is the layer coupling factor $-\gamma_1$ in the off-diagonal 4×4 blocks of the Hamiltonian. From the structure of H_c, one can easily see that no terms with factor $-\gamma_1$ can appear in the determinant when the Fermi energy is set to zero. Thus the determinant of the two systems are the same, and therefore the relations between the eigenvalues coincide. The eigenmodes corresponding to these eigenvalues have also been found with Mathematica, and are expressed in terms of ξ_v as:

$$\chi_v^+ = \big(0,0,0,0,1+\xi_v,0,-1,0\big)^T, \quad \chi_v^- = \big(0,\xi_v,0,-1-\xi_v,0,0,0,0\big)^T \tag{3.18}$$

These are quite similar to the ones found in graphene. The two distinct eigenmodes in graphene had one of them located on the A-sublattice, and the other on the B-sublattice. The same is found here, but now the modes also differ in layer: one is completely on the B-sublattice of the upper layer, and the other on the A-sublattice of the lower one.

Depending on the eigenvalues $\lambda_v^\pm$, the eigenmodes are divided into two categories (i.e. the distinguishment in eigenmodes mentioned earlier): the *propagating modes* for $\lambda_v^\pm = 1$, and *evanescent modes* for other values. It is easily seen that the propagating modes are only found when the k_x-momenta align perfectly with the K-valleys, where $\xi_{\mathbf{K}} = e^{2\pi i/3}$ and $\xi_{\mathbf{K'}} = e^{-2\pi i/3}$. Thus there are four propagating modes on every lead unit cell, which is described using the following matrices:

$$\Phi_{\text{pr}} = (\chi_{\mathbf{K}}^-, \chi_{\mathbf{K}}^+, \chi_{\mathbf{K'}}^-, \chi_{\mathbf{K'}}^+), \quad \Xi_{\text{pr}} = \text{diag}(\xi_{\mathbf{K}}, \xi_{\mathbf{K}}, \xi_{\mathbf{K'}}, \xi_{\mathbf{K'}}), \quad \Lambda_{\text{pr}} = \mathbb{1}_4 \tag{3.19}$$

It is clear that the matrix Λ_{pr} also has the eigenvalues of the translation operator in the y-direction on its diagonal, since they are all 1 for propagating modes. These matrices are used to construct the full set of propagating modes on lead cell m:

$$\Psi_{\text{pr}}\Lambda_{\text{pr}} = \begin{pmatrix} \Phi_{\text{pr}}\Xi_{\text{pr}}^{N-1} \\ \vdots \\ \Phi_{\text{pr}}\Xi_{\text{pr}} \\ \Phi_{\text{pr}} \end{pmatrix} \Lambda_{\text{pr}} \tag{3.20}$$

These propagating modes need to be separated in the incoming and outgoing modes. In the graphene paper, this is done using the *particle current operator* J, which is defined as:

$$J = \frac{2a}{\hbar}\text{Im}(\Lambda_{\text{pr}}^* T_L) \tag{3.21}$$

There is a problem that causes this method of separating states not to be usable in bilayer graphene. It is known from the previous section that in bilayer graphene systems, the dispersion relation is parabolic around the K-points. It is also true in general for electrons that their Fermi velocity equals the slope of the dispersion relation. This means that electrons near the bottom of the parabolas have a Fermi velocity of almost zero, and even exactly zero if the energy is zero as well. However, as the diagonalized version of the particle current operator $J_{pr} = \Psi_{pr}^\dagger J \Psi_{pr}$ is proportional to the Fermi velocity v_F, this matrix will always be zero. In graphene the eigenvectors of this matrix were used to separate the modes, which can't be done now. The first attempt at circumventing this problem was taking an infinitesimal energy ϵ instead of zero, and calculating the possible modes for that. This approach turned out to be impractical: the four distinct eigenvalues λ_v contained over thirty terms, and the eigenmode calculation required a week before hitting memory errors.

Therefore another method must be used to separate the modes. To not lose generality, a simple superposition of the four possible modes was mades, which looks similar to that of graphene. Then the superposing vectors $\eta_{\mathbf{K}}^- = \frac{1}{\sqrt{2}}(\alpha,1,0,0)^T$, $\eta_{\mathbf{K'}}^- = \frac{1}{\sqrt{2}}(0,0,\beta,1)^T$ are used for the incoming modes, and $\eta_{\mathbf{K}}^+ = \frac{1}{\sqrt{2}}(-\alpha,1,0,0)^T$, $\eta_{\mathbf{K'}}^+ = \frac{1}{\sqrt{2}}(0,0,-\beta,1)^T$ for the outgoing modes. The labelling **K** and **K'** can be used here as the eigenmodes χ

are distinct in valley as well. Note that these are similar to graphene, but firstly the vectors are not the eigenmodes of the current operator. Furthermore, the parameter α and β are introduced, which can take any value. In graphene the value is chosen such that the lead eigenmodes carry the same probability current. Here one could chose the parameters per example in a way that the incoming and outgoing modes are orthogonal, or take $\alpha = e^{\pi i/6}$ and $\beta = -\alpha^*$ to copy the graphene analysis. The superscript * here means the conjugate value. These vectors are now used to construct the incoming and outgoing propagating modes:

$$\Phi_{\text{in}} = \Phi_{\text{pr}}(\eta^-_{\mathbf{K}}, \eta^-_{\mathbf{K'}})/\sqrt{N}, \quad \Xi_{\text{in}} = \text{diag}(\xi_{\mathbf{K}}, \xi_{\mathbf{K'}}), \quad \Lambda_{\text{in}} = \mathbb{1}_2 \tag{3.22}$$

$$\Phi_{\text{out}} = \Phi_{\text{pr}}(\eta^+_{\mathbf{K'}}, \eta^+_{\mathbf{K}})/\sqrt{N}, \quad \Xi_{\text{out}} = \text{diag}(\xi_{\mathbf{K'}}, \xi_{\mathbf{K}}), \quad \Lambda_{\text{out}} = \mathbb{1}_2 \tag{3.23}$$

One key difference in the construction of the incoming and outgoing modes is the sorting. The order of the valleys is swapped, to ensure that there time-reversal symmetry still holds as it should, which was discussed shortly in the previous section. The final wavefunctions of the incoming and outgoing propagating modes are now:

$$(\psi^{\text{in}}_{\mathbf{K}}(m), \psi^{\text{in}}_{\mathbf{K'}}(m)) = \Psi_{\text{in}}\Lambda^m_{\text{in}} = \begin{pmatrix} \Phi_{\text{in}}\Xi^{N-1}_{\text{in}} \\ \vdots \\ \Phi_{\text{in}}\Xi_{\text{in}} \\ \Phi_{\text{in}} \end{pmatrix} \Lambda^m_{\text{in}} \tag{3.24}$$

$$(\psi^{\text{out}}_{\mathbf{K'}}(m), \psi^{\text{out}}_{\mathbf{K}}(m)) = \Psi_{\text{out}}\Lambda^m_{\text{out}} = \begin{pmatrix} \Phi_{\text{out}}\Xi^{N-1}_{\text{out}} \\ \vdots \\ \Phi_{\text{out}}\Xi_{\text{out}} \\ \Phi_{\text{out}} \end{pmatrix} \Lambda^m_{\text{out}} \tag{3.25}$$

The remaining modes were called the evanescent modes, where the eigenvalue $\lambda^\pm_v \neq 1$. Thus $-N/3 < v < N/3$ or $N/3 < v < 2N/3$, as there is a distinct number of modes possible. For the first of those two regimes it follows that $\lambda^-_v < 1$ and $\lambda^+_v > 1$. That means that the χ^+_v-modes are not normalisable, as their values will go to infinity if it is translated into the lead enough. Had the system been finite, then these would be proper modes: the χ^+_v-modes would be modes localised on the other side of the system. The χ^-_v-modes are normalisable however, and therefore allowed evanescent modes. In the second regime the reverse happens: χ^+_v-modes are allowed and χ^-_v-modes are not, again because of the normalisation. The construction of the evanescent wavefunctions now is analogous to what has been done previously, but with more distinct modes:

$$(\psi^{\text{ev}}_{-N/3+1}(m), \ldots, \psi^{\text{ev}}_{N/3-1}(m), \psi^{\text{ev}}_{N/3+1}(m), \ldots, \psi^{\text{ev}}_{2N/3-1}(m)) = (\Psi^-_{\text{ev}}\Lambda^-_{\text{ev}}, \Psi^+_{\text{ev}}\Lambda^+_{\text{ev}}) = \Psi_{\text{ev}}\Lambda_{\text{ev}} \tag{3.26}$$

$$\Psi^+_{\text{ev}} = \frac{1}{\sqrt{N}}\begin{pmatrix} \Phi^+_{\text{ev}}(\Xi^+_{\text{ev}})^{N-1} \\ \vdots \\ \Phi^+_{\text{ev}}\Xi^+_{\text{ev}} \\ \Phi^+_{\text{ev}} \end{pmatrix}, \quad \Psi^-_{\text{ev}} = \frac{1}{\sqrt{N}}\begin{pmatrix} \Phi^-_{\text{ev}}(\Xi^-_{\text{ev}})^{N-1} \\ \vdots \\ \Phi^-_{\text{ev}}\Xi^-_{\text{ev}} \\ \Phi^-_{\text{ev}} \end{pmatrix}, \quad \Lambda_{\text{ev}} = \text{diag}(\Lambda^-_{\text{ev}}, \Lambda^+_{\text{ev}}) \tag{3.27}$$

$$\begin{aligned} &\Phi^-_{\text{ev}} = (\chi^-_{-N/3+1}, \ldots, \chi^-_{N/3-1}), \quad \Xi^-_{\text{ev}} = (\xi_{-N/3+1}, \ldots, \xi_{N/3-1}), \quad \Lambda^-_{\text{ev}} = (\lambda^-_{-N/3+1}, \ldots, \lambda^-_{N/3-1}), \\ &\Phi^+_{\text{ev}} = (\chi^+_{N/3+1}, \ldots, \chi^+_{2N/3-1}), \quad \Xi^+_{\text{ev}} = (\xi_{N/3+1}, \ldots, \xi_{2N/3-1}), \quad \Lambda^+_{\text{ev}} = (\lambda^+_{N/3+1}, \ldots, \lambda^+_{2N/3-1}) \end{aligned} \tag{3.28}$$

The zero-energy assumption results in two incoming and two outgoing modes, which in turn makes the scattering matrix 2×2. Its parametrization will be done the same as in graphene, being:

$$S = e^{i\phi}\begin{bmatrix} re^{i\Delta} & \sqrt{1-r^2} \\ \sqrt{1-r^2} & -re^{-i\Delta} \end{bmatrix} \tag{3.29}$$

Three new real parameters r, ϕ and Δ are introduced here, the important of which is ϕ. That one is called the *scattering phase*, and equals the phase difference of a wave after being reflected. In a clean zigzag system, i.e. where there is no disorder on the boundary, the scattering matrix is the Pauli sigma-x matrix $\sigma_x = \begin{bmatrix} 0 & 1 \\ 1 & 0 \end{bmatrix}$ times a factor with a phase shift for the wavefunctions. This phase shift is the scattering phase, and is a consequence of being reflected. The same effect occurs when photons are reflected off of a surface with a

relatively high refractive index, where the phase shift is always π radians. To find the scattering matrix, a scattering state in the lead is composed using the eigenstates of an infinite system:

$$\Psi_L(m) = (\psi_{\mathbf{K}}(m), \psi_{\mathbf{K}'}(m)) = \Psi_{\text{in}}\Lambda_{\text{in}}^m + \Psi_{\text{out}}\Lambda_{\text{out}}^m S + \Psi_{\text{ev}}\Lambda_{\text{ev}}^m S_{\text{ev}} \tag{3.30}$$

This scattering state can be interpreted as the sum of an incoming wavefunction in a single valley, the possible reflected outgoing wavefunctions corresponding to that incoming mode, and evanescent modes. The matrix S_{ev} gives the amplitudes of scattering into those evanescent modes, just like the regular scattering matrix. Note that there are more evanescent modes than propagating modes when $N \geq 6$, so the matrix S_{ev} is *not* 2×2. Ordering the boundary wavefunctions $\Psi_B = (\psi_{B,\mathbf{K}}, \psi_{B,\mathbf{K}'})$ in the same way as Ψ_L by valley, the last two blocks of the the Schrödinger equation $H\begin{pmatrix}\Psi_L \\ \Psi_B\end{pmatrix} = 0$, with the Hamiltonian defined as in equation 3.9, gives the following:

$$\begin{bmatrix} \ddots & & & \\ & \ddots & & \\ & T_L^\dagger & H_L & T_{LB} \\ & & T_{LB}^\dagger & H_B \end{bmatrix} \begin{pmatrix} \vdots \\ \Psi_L(2) \\ \Psi_L(1) \\ \Psi_B \end{pmatrix} = 0 \tag{3.31}$$

The first two scattering states in the lead are found by filling in equation 3.30 and using the other definitions above, giving:

$$\begin{aligned} \Psi_L(1) &= \Psi_{\text{in}}\Lambda_{\text{in}} + \Psi_{\text{out}}\Lambda_{\text{out}} S + \Psi_{\text{ev}}\Lambda_{\text{ev}} S_{\text{ev}} \\ \Psi_L(2) &= \Psi_{\text{in}}\Lambda_{\text{in}}^2 + \Psi_{\text{out}}\Lambda_{\text{out}}^2 S + \Psi_{\text{ev}}\Lambda_{\text{ev}}^2 S_{\text{ev}} \end{aligned} \tag{3.32}$$

Writing out the two sums of the last two blocks of equation 3.31 using the definitions of the scattering states 3.32 brings forth the following set of equations:

$$\begin{cases} T_L^\dagger \Psi_{\text{in}}\Lambda_{\text{in}}^2 + T_L^\dagger \Psi_{\text{out}}\Lambda_{\text{out}}^2 S + T_L^\dagger \Psi_{\text{ev}}\Lambda_{\text{ev}}^2 S_{\text{ev}} + H_L \Psi_{\text{in}}\Lambda_{\text{in}} + H_L \Psi_{\text{out}}\Lambda_{\text{out}} S + H_L \Psi_{\text{ev}}\Lambda_{\text{ev}} S_{\text{ev}} + T_{LB}\Psi_B = 0 \\ T_{LB}^\dagger \Psi_{\text{in}}\Lambda_{\text{in}} + T_{LB}^\dagger \Psi_{\text{out}}\Lambda_{\text{out}} S + T_{LB}^\dagger \Psi_{\text{ev}}\Lambda_{\text{ev}} S_{\text{ev}} + H_B \Psi_B = 0 \end{cases} \tag{3.33}$$

The next step is then rewriting those equation into a matrix-vector multiplication, where the vector contains the sought-after matrix S. This method yields:

$$\begin{bmatrix} T_L^\dagger \Psi_{\text{out}}\Lambda_{\text{out}}^2 + H_L \Psi_{\text{out}}\Lambda_{\text{out}} & T_L^\dagger \Psi_{\text{ev}}\Lambda_{\text{ev}}^2 + H_L \Psi_{\text{ev}}\Lambda_{\text{ev}} & T_{LB} \\ T_{LB}^\dagger \Psi_{\text{out}}\Lambda_{\text{out}} & T_{LB}^\dagger \Psi_{\text{ev}}\Lambda_{\text{ev}} & H_B \end{bmatrix} \begin{pmatrix} S \\ S_{\text{ev}} \\ \Psi_B \end{pmatrix} = \begin{pmatrix} -T_L^\dagger \Psi_{\text{in}}\Lambda_{\text{in}}^2 - H_L \Psi_{\text{in}}\Lambda_{\text{in}} \\ -T_{LB}^\dagger \Psi_{\text{in}}\Lambda_{\text{in}} \end{pmatrix} \tag{3.34}$$

This system can be simplified even further, using the Schrödinger equation in the lead (see equation 3.12 with $E = 0$). The definition of the infinite lead wavefunctions then follows from the tight binding model, being $\psi_L^{\text{inf}}(m) = \Psi_\circ \Lambda_\circ^m$. The circles can stand for incoming, outgoing or evanescent modes. Applying this simplification and multiplying the upper row with -1 yields the following simplified set of equations:

$$\begin{bmatrix} T_L \Psi_{\text{out}} & T_L \Psi_{\text{ev}} & T_{LB} \\ T_{LB}^\dagger \Psi_{\text{out}}\Lambda_{\text{out}} & T_{LB}^\dagger \Psi_{\text{ev}}\Lambda_{\text{ev}} & H_B \end{bmatrix} \begin{pmatrix} S \\ S_{\text{ev}} \\ \Psi_B \end{pmatrix} = \begin{pmatrix} -T_L \Psi_{\text{in}} \\ -T_{LB}^\dagger \Psi_{\text{in}}\Lambda_{\text{in}} \end{pmatrix} \tag{3.35}$$

A lot of information is stored in this set, while the only goal is describing S. Therefore, a *discrete Fourier transform*[16] is applied to the system, which will eliminate a lot of terms. Since the equations are in the form of a matrix-vector multiplication, it has to be multiplied from the left with a variation of a *DFT*-matrix. The transformation should be applied to all sites within the wavefunctions, and therefore the following matrix is used:

$$\mathscr{U} = \begin{bmatrix} U \otimes \mathbb{1}_8 & 0 \\ 0 & U \otimes \mathbb{1}_4 \end{bmatrix}, \quad U = \frac{1}{\sqrt{N}} \begin{bmatrix} 1 & 1 & 1 & \cdots & 1 \\ 1 & \omega & \omega^2 & \cdots & \omega^{N-1} \\ 1 & \omega^2 & \omega^4 & \cdots & \omega^{2(N-1)} \\ \vdots & \vdots & \vdots & \ddots & \vdots \\ 1 & \omega^{N-1} & \omega^{2(N-1)} & \cdots & \omega^{(N-1)(N-1)} \end{bmatrix}, \quad \omega = e^{2\pi i/N} \tag{3.36}$$

One can check that each element of U indeed equals $U_{mn} = e^{2\pi i(N-m)(N-n)/N}$, so it correctly applies a discrete Fourier transform. The $\otimes$ in the definition of $\mathscr{U}$ denotes the *Kronecker product*[17]: For any matrices A and B, this product generates a matrix $C = A \otimes B$, such that the elements of C are defined as $C_{mn} = a_{mn}B$, where a_{mn} is the element in the m-th row and n-th column of A. The first row in equation 3.35 contains only wavefunctions from the lead, which describe eight atoms, and the second row contains boundary wavefunction which describe four atoms. Hence the Kronecker product is taken with the 8×8 and 4×4 identities respectively, to ensure that the transformation is performed on each site individually.

Now the transformation can be applied, by multiplying the equation from the left with $\mathscr{U}$. Each individual block of this multiplication was computed explicitly using Mathematica [15]. Note that the evanescent modes are split into three categories, to emphasise which terms cancel out exactly:

$$\left[\begin{array}{cccc|c} 0 & 0 & 0 & 0 & \\ -A_2 & 0 & 0 & 0 & \\ 0 & 0 & 0 & \Lambda^+_{\text{ev}} & (\mathbb{1}+\Xi^\dagger)\otimes T^B_y \\ -A_1 & 0 & 0 & 0 & \\ 0 & 0 & 0 & 0 & \\ \hline 0 & 0 & \Xi^{->}_{\text{ev}} & 0 & \\ e^{-\pi i/3}\alpha A_2 & 0 & 0 & 0 & \\ 0 & 0 & 0 & 0 & U_4 H_B U_4^\dagger \\ e^{\pi i/3}\beta A_1 & 0 & 0 & 0 & \\ 0 & \Xi^{-<}_{\text{ev}} & 0 & 0 & \end{array}\right] \begin{pmatrix} S \\ S^{-<}_{\text{ev}} \\ S^{->}_{\text{ev}} \\ S^{+}_{\text{ev}} \\ U_4\Psi_B \end{pmatrix} = \left(\begin{array}{c} 0 \\ A_1 \\ 0 \\ A_2 \\ 0 \\ \hline 0 \\ e^{-\pi i/3}\alpha A_1 \\ 0 \\ e^{\pi i/3}\beta A_2 \\ 0 \end{array}\right) \tag{3.37}$$

The new matrices here are:

$$A_1 = (\frac{1}{\sqrt{2}}, 0), \quad A_2 = (0, \frac{1}{\sqrt{2}}), \quad U_4 = U \otimes \mathbb{1}_4 \tag{3.38}$$

$$\begin{gathered} \Xi^{-<}_{\text{ev}} = \text{diag}(\xi_{-N/3+1}, \ldots, \xi_0), \quad \Xi^{->}_{\text{ev}} = \text{diag}(\xi_1, \ldots, \xi_{N/3-1}), \\ \Xi = \text{diag}(\xi_1, \ldots, \xi_N) = \text{diag}(\Xi^{->}_{\text{ev}}, \xi_{\mathbf{K}}, \Xi^{+}_{\text{ev}}, \xi_{\mathbf{K'}}, \Xi^{-<}_{\text{ev}}) \end{gathered} \tag{3.39}$$

Note that the upper right block of the first matrix equals $U_8 T_{LB} U_4^\dagger$ and not $U_8 T_{LB}$, as the DFT-4-matrix was appended in the last element of the vector it is multiplied with. The conjugate transpose of U is used here instead of the inverse as U is unitary. The paper about graphene this work is based on does not state the presence of the Kronecker product in this block explicitly. This is justified however by the fact that the other elements were zeroes anyways, and they were omitted immediately. Due to the reordering later however, this lack of included zeroes does not have influence on the original result, except that some notation should be a little different. To reflect the initial analysis, all columns and rows with only zeroes will not be denoted in the remainder here as well. Furthermore, the matrices $S^{-<}_{\text{ev}}$, $S^{->}_{\text{ev}}$ and S^{+}_{ev} are built so they can be used for the same ranges of momentum as the modified Ξ-matrices. It is also important to realise that the zeroes that are still left in these matrices are actually matrices with only zeroes. The sizes of these matrices can be deducted from the elements in the same column and row, or what it is multiplied with.

Luckily, this system is again very similar to the graphene case. Taking $\alpha = e^{\pi i/6}$ and $\beta = -\alpha^*$ as mentioned before yields the same parameters before the A_1's and A_2's in both the matrix on the left and the vector on the right. An important difference is the lower right block of the matrix, since the matrix H_B does not only contain information about the disordered boundary sites now. It can be calculated explicitly again, resulting in:

$$U_4 H_b U_4^\dagger = \begin{bmatrix} \tilde{V}_{0,0} & \tilde{V}_1 & \cdots & \tilde{V}_{N-1} \\ \tilde{V}_1{}^\dagger & \tilde{V}_{0,1} & \ddots & \vdots \\ \vdots & \ddots & \ddots & \tilde{V}_1 \\ \tilde{V}_{N-1}^\dagger & \cdots & \tilde{V}_1^\dagger & \tilde{V}_{0,N-1} \end{bmatrix}, \quad \tilde{V}_k = \frac{1}{N} \begin{bmatrix} 0 & 0 & 0 & 0 \\ 0 & 0 & 0 & 0 \\ 0 & 0 & 0 & 0 \\ 0 & 0 & 0 & \sum_{j=0}^{N-1} V_j e^{2\pi i(j-1)k/N} \end{bmatrix},$$
$$\tilde{V}_{0,k} = \begin{bmatrix} 0 & 0 & -\gamma_1 & 0 \\ 0 & 0 & -\gamma_0 & 0 \\ -\gamma_1 & -\gamma_0 & 0 & -\gamma_0 - \xi_{-(k+1)} \\ 0 & 0 & -\gamma_0 - \xi_{k+1} & \frac{1}{N}\sum_{j=0}^{N-1} V_j \end{bmatrix} \tag{3.40}$$

The bottom right element of all the $\tilde{V}$-matrices contain the Fourier coefficients of the disorder potential on the boundary sites, as seen in their definitions. Since there are other non-distorted sites in the boundary wavefunctions, hopping energies γ_0 and γ_1 still appear in the $\tilde{V}$-matrices on the diagonal, along with terms that resemble hoppings in the x-direction. These other terms do not seem to interfere with the calculations later on however, so the similarity with graphene prevails. This also justifies leaving out those columns and rows in the rest of this analysis, such that the onsite disorder matrices $\tilde{V}_k$ contain just the disordered sites. The original notation of those matrices will still be used instead of just the disorder potential however, to signify the distinctness of this analysis to that of graphene. The next step is rewriting equation 3.37 by pivoting in a smart way: it yields a block-diagonal matrix where one part does not depend on S_{ev}, which isn't as informative as S itself. It is found that this new system can be rewritten as:

$$\begin{bmatrix} \bar{V} & B_1 \\ C & D_1 \end{bmatrix} \begin{pmatrix} \bar{\Psi} \\ S \end{pmatrix} = \begin{pmatrix} B_2 \\ D_2 \end{pmatrix} \tag{3.41}$$

The upper element in the first vector $\bar{\Psi}$ will be annihilated in the way how S is found, and therefore its structure will not be elaborated on further. The other matrices in this equation are as follows:

$$\bar{V} = \left[\begin{array}{ccc|cc} \tilde{V}_{0,1} & \cdots & \tilde{V}_{N/3-2} & \tilde{V}_1^\dagger & \tilde{V}_{N/3-1} \\ \vdots & \ddots & \vdots & \vdots & \vdots \\ \tilde{V}_{N/3-2}^\dagger & \cdots & \tilde{V}_{0,N/3-1} & \tilde{V}_{N/3-1}^\dagger & \tilde{V}_1 \\ \hline \tilde{V}_1 & \cdots & \tilde{V}_{N/3-1} & \tilde{V}_{0,0} & \tilde{V}_{N/3} \\ \tilde{V}_{N/3-1}^\dagger & \cdots & \tilde{V}_1^\dagger & \tilde{V}_{N/3}^\dagger & \tilde{V}_{0,N/3} \end{array}\right], \quad C = \left[\begin{array}{ccc|cc} 0 & \cdots & 0 & 1+\xi_{\mathbf{K}'} & 0 \\ 0 & \cdots & 0 & 0 & 1+\xi_{\mathbf{K}} \end{array}\right],$$

$$B_1 = \left[\begin{array}{cc} 0 & 0 \\ \vdots & \vdots \\ 0 & 0 \\ \hline 0 & \frac{e^{-\pi i/3}\alpha}{\sqrt{2}} \\ \frac{e^{\pi i/3}\beta}{\sqrt{2}} & 0 \end{array}\right], \quad B_2 = \left[\begin{array}{cc} 0 & 0 \\ \vdots & \vdots \\ 0 & 0 \\ \hline \frac{e^{-\pi i/3}\alpha}{\sqrt{2}} & 0 \\ 0 & \frac{e^{\pi i/3}\beta}{\sqrt{2}} \end{array}\right], \quad D_1 = \begin{bmatrix} 0 & -\frac{1}{\sqrt{2}} \\ -\frac{1}{\sqrt{2}} & 0 \end{bmatrix}, \quad D_2 = \begin{bmatrix} \frac{1}{\sqrt{2}} & 0 \\ 0 & \frac{1}{\sqrt{2}} \end{bmatrix} \tag{3.42}$$

In the matrix $\bar{V}$, only the first third of the Fourier coefficients of the disorder potential V can be found. To solve equation 3.41 for S, a trick called *block matrix inversion*[18] is used. The assumption that $\bar{V}$ and D_1 are invertible has to be made, the second of which is easy to see, and the first will follow later. Utilising this, both sides of the equation can be multiplied from the left with the inverse of the first matrix, which according to this trick equals:

$$\begin{bmatrix} \bar{V} & B_1 \\ C & D_1 \end{bmatrix}^{-1} = \begin{bmatrix} \bar{V}^{-1} + \bar{V}^{-1}B_1(D_1 - C\bar{V}^{-1}B_1)^{-1}C\bar{V}^{-1} & -\bar{V}^{-1}B_1(D_1 - C\bar{V}^{-1}B_1)^{-1} \\ -(D_1 - C\bar{V}^{-1}B_1)^{-1}C\bar{V}^{-1} & -(D_1 - C\bar{V}^{-1}B_1)^{-1} \end{bmatrix} \tag{3.43}$$

This might look even more complicated at first glance, but do remember that the equation only needs to be solved for S. That problem is now reduced to the inverse of $\bar{V}$. This can be seen by rewriting the bottom row of equation 3.41 with the multiplication from the left:

$$S = (D_1 - C\bar{V}^{-1}B_1)^{-1}(D_2 - C\bar{V}^{-1}B_2) \tag{3.44}$$

Furthermore, the matrix C and both B-matrices only have nonzero elements in their last two columns and rows respectively. Thus only the lower right 2×2 block of $\bar{V}^{-1}$ has to be found to solve this entire problem. This lower right matrix is denoted as W, which is Hermitian as $\bar{V}$ is also Hermitian by looking at its definition. The elements of W are denoted as follows:

$$\bar{V}^{-1} = \left[\begin{array}{ccc|cc} \ddots & & & \ddots & \\ & \ddots & & & \ddots \\ \hline \ddots & & & W_{11} & W_{12} \\ & \ddots & & W_{21} & W_{22} \end{array}\right] \tag{3.45}$$

One last trick has to be used to find this matrix W, with which the matrix S can be expressed. The so-called *Schur complement*[19] is used, for which the four blocks of $\bar{V}$ split by lines will now be called $\bar{V}_{11}$, $\bar{V}_{12}$, $\bar{V}_{21}$ and $\bar{V}_{22}$. It is utilised in the following manner:

$$W = (\bar{V}/\bar{V}_{11})^{-1}, \quad \bar{V}/\bar{V}_{11} := \bar{V}_{22} - \bar{V}_{21}\bar{V}_{11}^{-1}\bar{V}_{12} \tag{3.46}$$

One can recognise this expression as a part of the block matrix inversion used earlier. To retrieve W from this, the block matrix inversion is used again. From that the scattering matrix S can finally be expressed in terms of $Y = W^{-1}$, which in its turn is expressed in the random boundary disorder potentials V. This matrix is structured in the following manner:

$$Y = \bar{V}_{22} - \bar{V}_{21}\bar{V}_{11}^{-1}\bar{V}_{12} = \begin{bmatrix} \tilde{V}_{0,0} & \tilde{V}_{N/3} \\ \tilde{V}_{N/3} & \tilde{V}_{0,N/3} \end{bmatrix} - \begin{bmatrix} \tilde{V}_1 & \cdots & \tilde{V}_{N/3-1} \\ \tilde{V}_{N/3-1}^\dagger & \cdots & \tilde{V}_1^\dagger \end{bmatrix} \begin{bmatrix} \tilde{V}_0 & \cdots & \tilde{V}_{N/3-2} \\ \vdots & \ddots & \vdots \\ \tilde{V}_{N/3-2}^\dagger & \cdots & \tilde{V}_{0,N/3-1} \end{bmatrix}^{-1} \begin{bmatrix} \tilde{V}_1^\dagger & \tilde{V}_{N/3-1} \\ \vdots & \vdots \\ \tilde{V}_{N/3-1}^\dagger & \tilde{V}_1 \end{bmatrix} \tag{3.47}$$

Filling in all the found parameters in equation 3.44 gives the following straightforward expression for the scattering matrix S:

$$S = \frac{1}{1-\det(Y)-2iY_{11}} \begin{bmatrix} -2e^{\pi i/3}\beta Y_{12}^* & 1+\det(Y) \\ 1+\det(Y) & -2e^{-\pi i/3}\alpha Y_{12}^* \end{bmatrix} \tag{3.48}$$

Obtaining the scattering phase from the scattering matrix is easy, using its definition given in equation 3.29. The angle of the upper right element of S equals the scattering phase, so:

$$\phi = \arg(S_{12}) = \arg\Big(\frac{1+\det(Y)}{1-\det(Y)+2iY_{11}}\Big) = \text{arctan2}(1-\det(Y), -2Y_{11}) \tag{3.49}$$

The function *arctan2(y,x)* here is an adjustment of the arctangent, making sure that it correctly returns the angle. The normal arctangent function does not correctly find angles when per example both x and y are negative. The arctan2-function is defined as the angle in the Euclidian plane between the positive x-axis and the vector (x, y).

To analyse the variance of this scattering angle, some assumptions will be made. First of all, the matrix $\tilde{V}_{11}$ should be dominated by its diagonal. This ensures its invertibility. Also, the random onsite potentials V_j will be parametrized by a mean value and a random fluctuating term, like this: $V_j = V_d + \delta V(j)$. The fluctuating term has a mean value of zero and a Gaussian correlation in space, such that the covariance equals $\text{Cov}[\delta V(j), \delta V(j') = s_d^2 e^{-\pi(j-j')^2/a^2}$ where s_d^2 is its variance. Now the Fourier coefficients of the random onsite potential are defined as found as:

$$\tilde{V}_k = V_d\delta_{k,0} + s_v x_k, \quad s_v = \frac{1+V_d^2}{2}s_d \tag{3.50}$$

The factor x_k here is a variable with zero mean and a variance of 1. The exact definition of x_k does not matter for the remainder of the derivation and will hence not be explored further. From this the matrix $\tilde{V}_{11}$ can be denoted as:

$$\tilde{V}_{11} = V_d\mathbb{1} + s_v\mathbf{x} \tag{3.51}$$

The matrix **x** here is now a random Toeplitz matrix from the elements x_k. Inverting this matrix is done by recognising the geometrical series, assuming that $s_v \propto s_d << V_d$. This assumption not only validates the usage of the geometrical series, but also ensures that the disordered edge-band does not overlap with the Fermi energy $E_F = 0$ here. The inverted matrix now looks like:

$$\tilde{V}_{11}^{-1} = \frac{1}{V_d}\Big(\mathbb{1} + \frac{s_v}{V_d}\mathbf{x}\Big)^{-1} = \frac{1}{V_d}\mathbb{1} - \frac{s_v}{V_d^2}\mathbf{x} + \mathcal{O}\Big(\frac{s_v^2}{V_d^2}\Big) \tag{3.52}$$

As the assumption states that $s_v << V_d$, the *Big O notation* $\mathcal{O}$ [20] is used. With this new definition of $\tilde{V}_{11}^{-1}$, the value of Y_{11} can be expressed in the following way:

$$Y_{11} = -V_d - s_v x_0 + \frac{s_v^2}{V_d}\sum_{n=1}^{\infty}|x_n|^2 + \mathcal{O}\Big(\frac{s_v^3}{V_d^3}\Big) \tag{3.53}$$

To obtain the variance of the scattering phase, the last simplification made is that $\det(Y) \approx Y_{11}^2$, which is appropriate as the matrix Y was stated to be dominated by its diagonal. Now ϕ will be expressed in terms of s_d (so *not* s_v) and V_d. Averaging over the fluctuating terms x_k, whose distribution is known, gives the following relation for the variance:

$$\mathrm{Var}(\phi) \propto \frac{s_d^2}{L} \tag{3.54}$$

This is indeed what the law of reflection predicts to happen: the variance of the scattering angle decreases when the boundary periodicity grows, i.e. when the boundary roughness decreases.

The geometrical series was used with the assumption that $s_d << V_d$, so now the opposite scenario is looked at shortly. In this case the disordered edge band does overlap with the Fermi energy, and under that condition diffusive scattering was found in graphene systems. An expression where ϕ is expressed in terms of L can again not be found, as the expression of $\tilde{V}_{11}$ in equation 3.51 can not be inverted generally. Thus a numerical analysis is done for a small system, and it is found that:

$$\mathrm{Var}(\phi) \propto s_d \tag{3.55}$$

The variance of the scattering phase analytically is the same as in graphene. Another thing to note is that the parameters α and β do not have any influence on the variance of the scattering phase, given that the four superposing vectors η are structured as they were. However, in the original graphene paper [2] the variance of the scattering phase was also derived using the continuum description. In this derivation a boundary condition was used that interpolated between a clean zigzag edge boundary and an infinite-mass boundary condition [21]. It was decided that this boundary condition can't be used for the bilayer graphene system, and hence another must be found to analyse the continuum model. These conditions were never the main focus of this work and are beyond the scope considering the time, and are therefore recommended as a future research.

Generally it is thought that the shape of $\mathrm{Var}(\phi)$ vs L and $\mathrm{Var}(\varphi)$ vs λ_F are the same, where φ is the scattering angle. Therefore the entire specularity and diffusivity of the reflections within bilayer graphene should coincide with that of graphene. This concludes the analysis of the tight-binding model, so now the details of the methods of the numerical simulations are presented.

3.2. Computation of the scattering angle

A semi-infinite system with periodic boundary conditions has now been built, from which the scattering matrix is needed to find the scattering angles of the modes. The scattering matrix is computed by Kwant in a way similar as described in the previous section about the tight-binding model. It identifies propagating and evanescent modes exactly the same, but then finds the matrix numerically instead of analytically. This method is pretty quick, but the basis in which it is returned is sub-optimal. The following basis change is used on the scattering matrix to get it in a preferable basis:

$$S \rightarrow P \cdot U \cdot V^T \cdot S \cdot V \cdot U \cdot P \tag{3.56}$$

This results in any composed scattering matrix to be returned as one with the same basis as the translation matrices. The three other matrices introduced in this transformation are needed for the following reasons:

– V: From the edge dispersion of bilayer graphene it is known that for a single value of k_y, two values of k_x differing in sign are allowed, in the two distinct valleys. The translation operator in the x-direction T_x is needed, which shifts modes one unit cell in the x-direction. Diagonalizing this operator in the subspace of two modes with the same k_y, say $|k_{y,1}\rangle$ and $|k_{y,2}\rangle$, gives:

$$T_{sub} = \begin{bmatrix} \langle k_{y,1}|T_x|k_{y,1}\rangle & \langle k_{y,1}|T_x|k_{y,2}\rangle \\ \langle k_{y,2}|T_x|k_{y,1}\rangle & \langle k_{y,2}|T_x|k_{y,2}\rangle \end{bmatrix} \tag{3.57}$$

This results in a matrix with eigenvalues $e^{\pm ik_x}$ and two eigenvectors $v_{y,1}$ and $v_{y,2}$. The matrix V used in the transformation is now a sparse matrix, with 2×2 eigenvector blocks $[v_{y,1}, v_{y,2}]$ on the diagonal for each mode. This all ensures that the scattering matrix is rotated into the eigenbasis of the translation operator.

– U: This matrix simply makes sure that every two modes with same momentum k_y are sorted in the same way. First the modes with positive k_x appear, then the ones with negative k_x. If the modes by chance are sorted perfectly, U is the identity matrix. For each two modes that are not in the right order, the 2×2 identity block corresponding to those modes is swapped with a matrix with the ones on the off-diagonal instead (which is equal to one of the Pauli matrices, σ_x). Do remember that the outgoing modes are sorted in the opposite valleys, as then time-reversal symmetry still holds.

– P: In the previous chapter it was stated that the system does not only have just mentioned time-reversal symmetry, but also chiral symmetry. The relevance of these symmetries is also shortly explained there. Ensuring that this symmetry holds for the modes reflected by the scattering matrix is done by fixing the phase, using matrix P.

The scattering matrix is now in the same basis as the translation operator. For the modes to be in the same basis, a similar transformation is used:

$$\psi \to U \cdot V^T \cdot \psi \tag{3.58}$$

The definitions of the matrices U and V ensure that wavefunctions with different values of k_x do not get mixed here. From these modes the angle of incidence can be calculated, by using their velocities in the x- and y-direction. The velocities are not just the momenta divided by the mass, as this is no classical setting. Instead, they are obtained by using the *Hellmann-Feynman theorem* [22]. This theorem states the following:

$$\frac{\mathrm{d}E}{\mathrm{d}q} = \langle \psi_q | \frac{\mathrm{d}H}{\mathrm{d}q} | \psi_q \rangle \tag{3.59}$$

Here H is the tight binding Hamiltonian, q is any continuous parameter, and the modes $|\psi\rangle$ are normalised. This normalisation is required to find the right ratio between the velocities: neglecting it will return skewed angles. In general, the velocity of the electrons within the system equals the slope of the dispersion. This fact can be stated as $\dfrac{\mathrm{d}E}{\mathrm{d}k_i} = v_i$, where i can be any direction. This is used in combination with the Hellmann-Feynman theorem to find the velocities. It follows that the x- and y-velocities are the expectation values of the velocity operators under the given wavefunction:

$$v_x = \langle \psi | V_x | \psi \rangle = i \cdot \langle \psi | T_x - T_x^\dagger + T_{xy} - T_{xy}^\dagger | \psi \rangle \tag{3.60}$$

$$v_y = \langle \psi | V_y | \psi \rangle = i \cdot \langle \psi | T_y - T_y^\dagger + T_{xy} - T_{xy}^\dagger | \psi \rangle \tag{3.61}$$

These velocity operators are the derivatives of the Hamiltonian to the momenta k_x and k_y, and the form used here is deducted from the tight binding model. These expectation values are now calculated using the known momenta of the modes, which are again related to the eigenvalues of the translation operators. The angles are then computed by taking the tangent of these two velocities. For a zigzag edged system, it was referenced that there are two k_x values per k_y value, at both K-valleys. This is shown in the next figure, where the locations of the plotted points indicate the allowed momenta of the incoming modes, and the arrows show the direction and magnitude of the velocities:

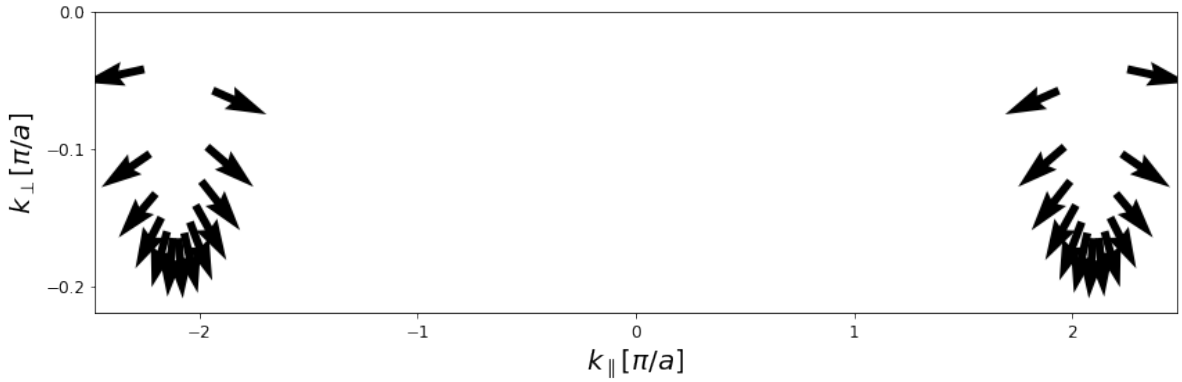

Figure 3.2: Quiverplot showing the allowed momenta in bilayer graphene, for $L = 240a$ and $E_F = 0.3t$. The momenta are indeed located around the two Dirac points. The arrows indicate the velocities corresponding to those momenta. Figure was made using Kwant [10].

The momenta and velocities of the outgoing modes can be depicted in the same way, where it would be exactly the same except for being mirrored in the k_x-axis. One can indeed see that the momenta are located around the two K-valleys, at $k_x = \pm 2\pi/3a$, and that the velocities point outward as they are the slope of the dispersion there. The velocities also all have approximately the same absolute values, as the dispersion relation is parabolic and therefore the magnitude of its slope is equal at the same height E_F. As told before, a second parabola appears as $E_F > \gamma_1$, which can be seen in the next figure:

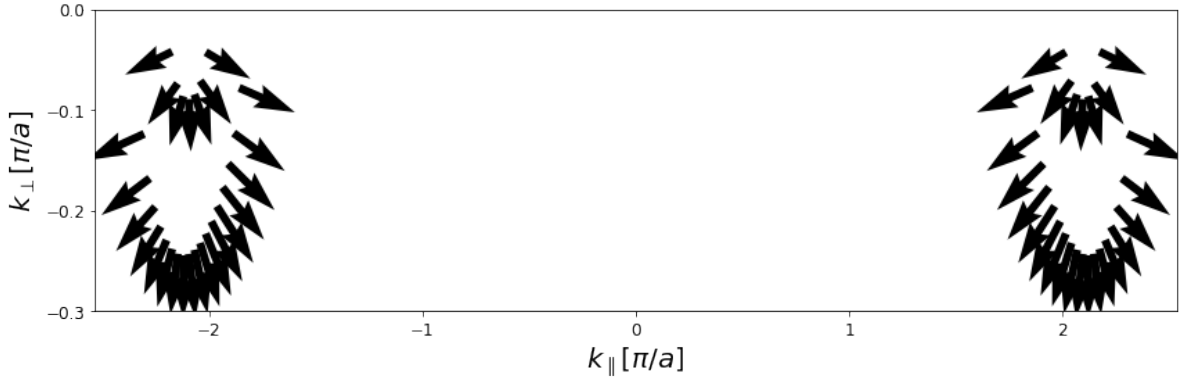

Figure 3.3: Quiverplot showing the allowed momenta in bilayer graphene, for $L = 240a$ and $E_F = 0.5t$. As the energy $E_F > \gamma_1$, a second ring of momenta shows up, stemming from the second parabola. The arrows indicate the velocities corresponding to those momenta. Figure was made using Kwant [10].

Two more circles of allowed momenta appear within the previous, as expected. Note that the scale of the $k_\perp$-axis is different: at higher energies the parabola spreads out, thus lower values of $k_\perp$ are allowed for the incoming modes.

It is now clear what steps need to be taken to get both the scattering angle and scattering phase from the tight-binding model. The next section introduces ways to analyse the specularity of those reflections, using variances.

3.3. Analysing the variance

The way the specularity and diffusivity of reflections is decided, is by looking at variances. A system is built in Kwant as described in the previous two sections, with a random variable placeholder on the boundary site potentials. For a set number of runs, a random disorder configuration is put on the outermost atoms, and for the entire system the scattering matrix is computed. Kwant does this by applying a numerical algorithm on the Schrödinger equation, and from the scattering matrix more information can be deducted.

Firstly, one can take the square of the absolute value of all the elements of the (properly ordered) scat-

tering matrix to find the probabilities of scattering from each incoming mode to each outgoing mode. The probability of specular intravalley reflections is then simply the average of the elements of the scattering matrix which connect modes with the same parallel momentum k_x. Then, the probability of diffusive intravalley scattering is the average of the probabilities of scattering within the same valley minus the probability of specular intravalley scattering. Note that these two probabilities don't add up to 1, as the intervalley scattering has not been taken into account yet. From these three probabilities one can also calculate other odds. For example, the total probability of scattering into another mode than the specular one can be found by adding the last two.

The variance of the scattering angle is computed using those same probabilities. Let P_{KK} contain the probabilities of scattering from incoming modes in valley K to outgoing modes in valley K, let $P_{K'K}$ contain the probabilities of scattering from incoming modes in valley K to outgoing modes in valley K', et cetera. Then make two vectors φ_K and $\varphi_{K'}$ with the angles of the modes, sorted in the same order as the probability matrices. For a certain incoming wave in valley K with angle φ_d with respect to the boundary, the mean intravalley outgoing angle $\tilde{\varphi}_{Kd}$ and the variance of that outgoing angle $\mathrm{Var}(\varphi_{Kd})$ are then:

$$\tilde{\varphi}_{Kd} = P_{KK}[:,d] \cdot \varphi_K, \quad \mathrm{Var}(\varphi_{Kd}) = P_{KK} \cdot (\tilde{\varphi}_d - \varphi_K)^2 \tag{3.62}$$

The notation $P_{KK}[:,d]$ here means the column of P_{KK} corresponding to the incoming mode with angle φ_d. In the same fashion the mean intervalley outgoing angle $\tilde{\varphi}_{K'd}$ and the variance of that scattering angle $\mathrm{Var}(\varphi_{K'd})$ can be calculated. Now the mean is taken over all the variances $\mathrm{Var}(\varphi_{Kd})$ and $\mathrm{Var}(\varphi_{K'd})$ for all incoming modes in both valleys, and the variance of the scattering angle $\mathrm{Var}(\varphi)$ is returned. By checking if this value either increases or decreases when another parameter changes, one can deduce whether the reflections become respectively more diffusive or more specular. It is important to realise that this variance is of a single system with one precise disorder configuration. Therefore it is important to average this variance over multiple disorder configurations as well, as one realisation can not indicate behaviour of all possible scenarios.

Something important to note here as well is that there are more allowed modes when the Fermi energy E_F is higher than the interlayer hopping parameter γ_1, as seen in figure 3.3. That means that it is possible to have two incoming modes with almost the exact same momentum parallel to the boundary $k_\parallel$. Even when no disorder is present in the system, incoming waves can scatter into ones with a different momentum parallel to the boundary $k_\perp$, that most likely has a slightly different angle as well. Thus another reason not to consider energies which exceed this limit in the remainder of this work.

Finding the value of the scattering phase numerically takes fewer steps than the analytical way. The energy of the system should be sufficiently low that there are only two possible incoming and two possible outgoing modes, which ensures that the scattering matrix is 2×2. Kwant finds small scattering matrices like these almost instantly. The scattering phase then equals the angle of one of the off-diagonal elements, using the parametrization from equation 3.29. Note that the basis change from the previous section needs to be performed before taking the angle.

This is all the required knowledge of how to compute the scattering angle and scattering phase in these systems, and how one can analyse those with respect to specularity. The results of countless numerical simulations which utilise these techniques are the next topic of discussion.

4

Results and Discussion

Readers who are interested in the code that generated these results are kindly referred to the repository on GitLab: https://gitlab.kwant-project.org/qt/RutgerE/broken-mirrors

4.1. Probability of specular and diffusive reflection

The expectation is that diffusive scattering commences when the edge band starts to overlap with the parabolic band. When the disorder mean V_d equals the Fermi energy, it should overlap for any disorder standard deviation s_d, which can be seen figure 4.1.

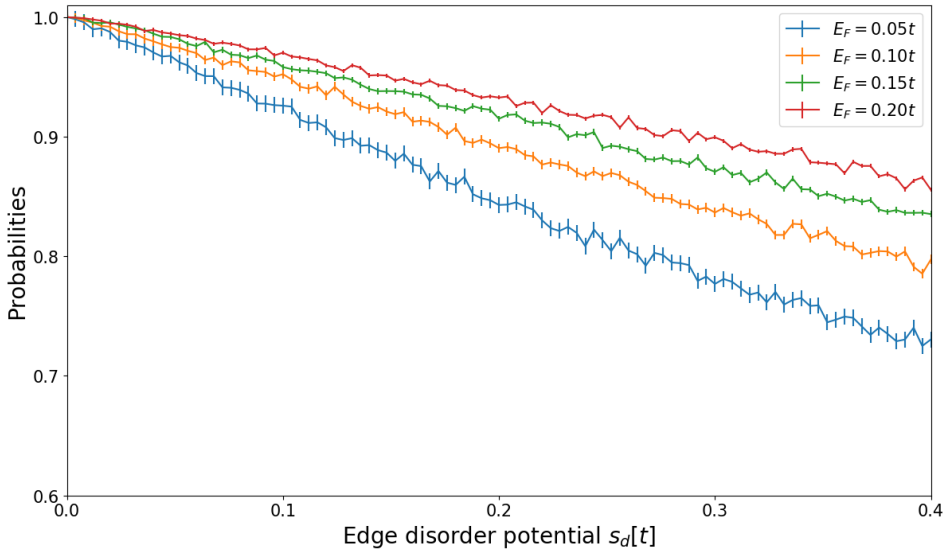

Figure 4.1: Probabilities of specular reflection for different Fermi energies and disorder strength, where the disorder mean $V_d = E_F$. Averaged over 1000 disorder configurations, with errorbars denoting the variances. The system used to generate this figure had a boundary periodicity of $L = 240$.

The probabilities of specular reflection indeed decrease instantly at finite disorder. It can be seen that lowering the Fermi energies steepen the decrease. This is logical when compared with the edge density of states, especially when looking at figure 2.9d. The overlap is larger at the bottom of the parabolas, and therefore more diffusive resonant edge scattering is expected.

For the next figure, the disorder mean was set to $V_d = E_F - 0.2t$. Now the diffusivity of the scattering only starts when the edge band is broad enough, as seen in figure 4.2.

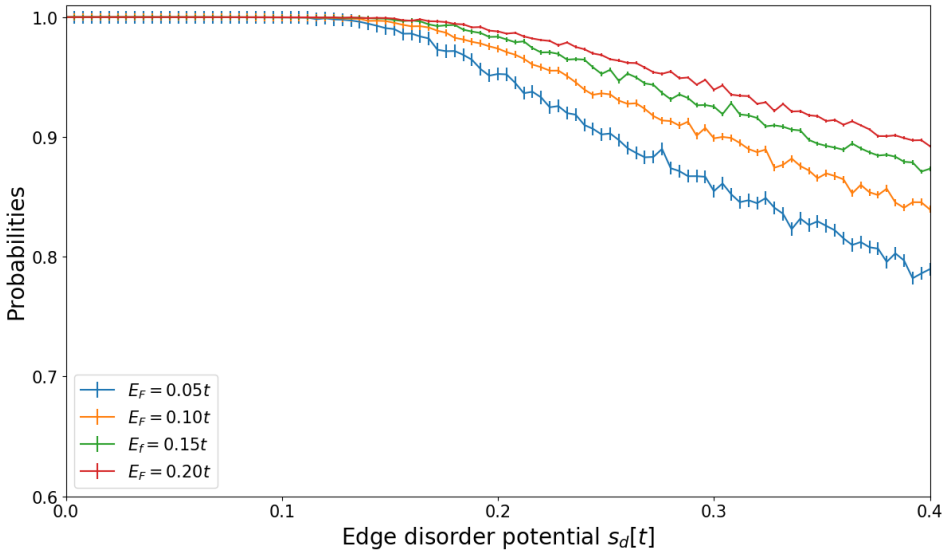

Figure 4.2: Probabilities of specular reflection for different Fermi energies and disorder strength, where the disorder mean $V_d = E_F - 0.2t$. Averaged over 1000 disorder configurations, with errorbars denoting the variances. The system used to generate this figure had a boundary periodicity of $L = 240a$.

Indeed, the diffusive scattering comes into play when the disorder is high enough to cross the gap between the edge states and the Fermi energy. Probabilities of diffusive scattering are simply 1 minus the probabilities of specular reflection. Therefore they were deemed not interesting enough to put here.

4.2. Variance of the scattering angle

Up until this point the behaviour of the reflections seems to be somewhat of a copy of graphene. This changes however when the scattering angle is looked at. To see where it differs, an image similar to figure (2b) of [2] was made, which is shown in figure 4.3.

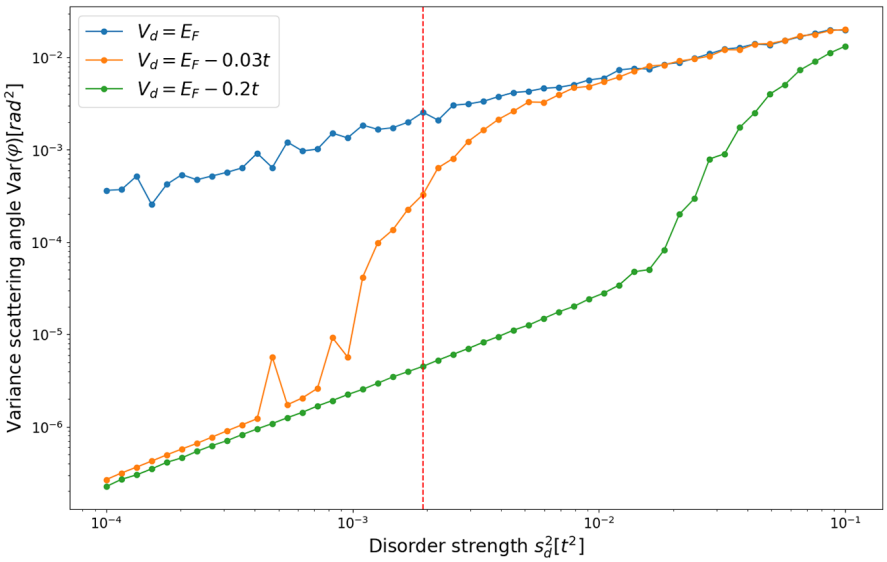

Figure 4.3: Variance of the scattering angle Var(φ) versus the disorder variance s_d^2, not the standard deviation as before. The energy of the electrons is $E_F = 0.2t$, which corresponds to a Fermi wavelength of $\lambda \approx 60a$. The boundary periodicity here is $L = 240a$, and it is averaged over 1000 runs. The dotted line indicates the value of s_d which is used in the next figure.

The variance of the scattering angle increases quadratically with the disorder strength s_d for all three disorder means. When $s_d \geq |V_d - E_F|$, the edge band should overlap with the Fermi energy, and different behaviour is expected. The middle line for $V_d = E_F - 0.03t$ clearly shows this, as it suddenly increases from

the disconnected band behaviour to connected band behaviour. For this value of disorder strength, denoted with a striped line in the figure and with value $s_d = 0.035t$, the variance was computed for different values of the Fermi energy. The Fermi energy was related to the Fermi wavelength by equation 2.7 for low energies, and since the law of reflection is described in wavelengths the following figure is expressed in it as well.

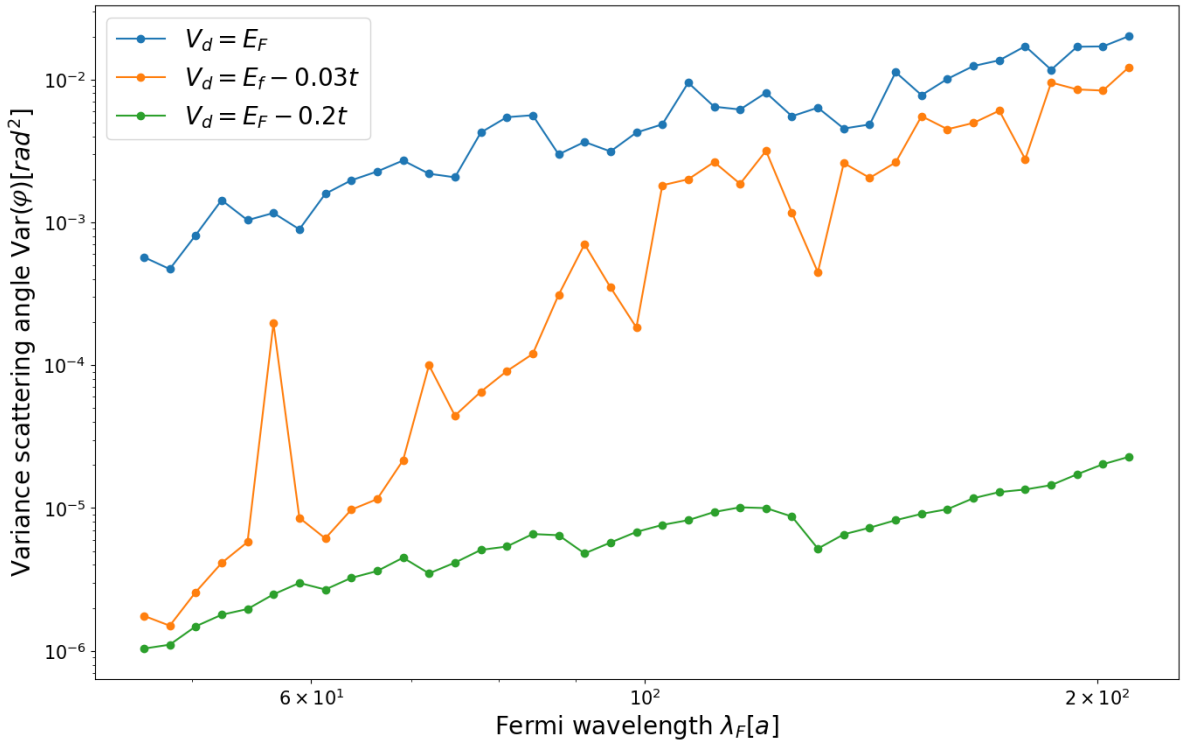

Figure 4.4: Variance of the scattering angle versus the Fermi wavelength. Used parameters are $s_d = 0.035t$, $L = 240a$, and it is averaged over 105 runs. The Fermi wavelengths correspond to Fermi energies between $0.3t$ and $0.02t$, decreasing from left to right.

This is the most surprising result up until now: the variance of the scattering angle increases with Fermi wavelength, independent of the distance between the corresponding Fermi energy and the disorder mean. As the wavelength increases with factor 2, the variance increases with factor 10. This increase of variance is therefore cubic in nature. For figure 4.4, more lines were generated with other distances between the Fermi energy and the disorder mean. This data followed the same trend as the ones plotted, where it coincided with these lines dependent on in what regime the distance was: If the distance was smaller than s_d, it followed the blue line, if it was roughly equal to s_d it followed the orange one, and if it was greater than s_d it followed the green one. Another thing to note are the small bumps in the lines, seen most clearly in the line for $V_d = E_F - 0.2t$. These are a consequence of the fact that the amount of allowed modes changes with the Fermi energy. The most right bump is per example caused by a sudden change from 14 to 10 different allowed incoming modes, which messes with the variance calculation. Nonetheless the trend of increasing variance is still very noticeable. This is surprising for multiple reasons.

- This trend does not only fail to follow the law of reflection, it actually even does the *exact opposite*. The found phenomenon expressed in terms of wavelength is: the diffusivity of the scattering increases when the wavelengths of the electrons increase. The reason for this will be narrowed down in the remainder.

- The variance of the scattering angle versus the Fermi wavelength was thought to be follow the same trend as the variance of the scattering phase versus the boundary periodicity / boundary roughness. The analytical derivation of the variance of the scattering phase using the tight-binding model in the previous chapter however states something else. It should be constant when the edge band overlaps with the Fermi energy, and decrease when it doesn't. Whether this analysis is right or not will be confirmed with numerical simulations as well. In graphene, these variances did follow the same trend, which distances the behaviour of bilayer graphene to that of monolayer.

Before the scattering phase is also calculated numerically to verify the analytical results, a way of avoiding the bumps in figure 4.4 has been devised. The variance of the scattering angle can be generated without them, as they are only a consequence of mode discontinuity. This problem is tackled by not only varying over the Fermi wavelength, but also the system size. By keeping the ratio between the two roughly constant, the number of modes can be kept constant over the entire energy regime. By trial and error, the following ratio between the two was found which kept the number of modes constantly at 14 in the regime $102 \leq L \leq 300$:

$$\lambda_F = \frac{\sqrt{3}\pi}{\sqrt{\left(0.37 - 0.3\left(\frac{L-102}{198}\right)^{0.65}\right)\frac{\gamma_1}{\gamma_0^2}}} \tag{4.1}$$

This equation is actually the dispersion relation from equation 2.7, with the Fermi energy term replaced with something dependent on the system size. This ratio comes down to $0.35L \leq \lambda_f \leq 0.45L$ which is sufficiently close to constant for this approach. The new figure without small bumps is depicted below.

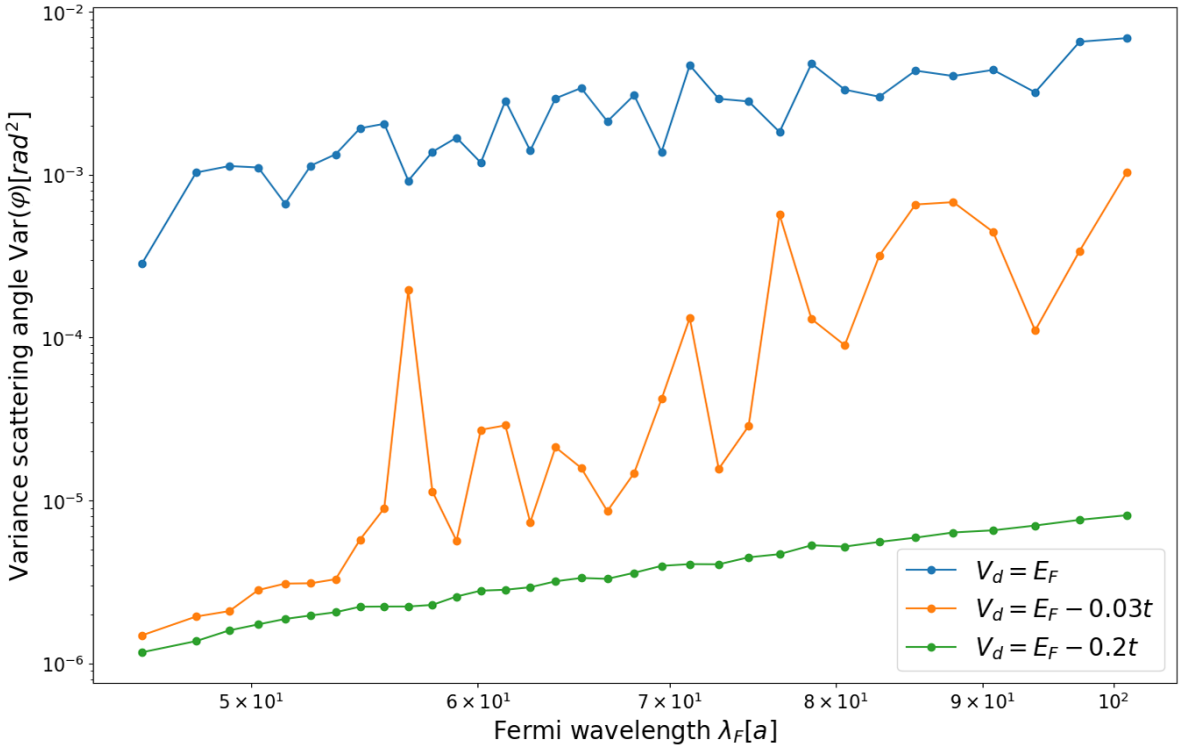

Figure 4.5: Variance of the scattering angle versus the Fermi wavelength, where the system size is roughly $L = 2.5\lambda_F$. Used parameters are $s_d^2 = 0.035t$, and it is averaged over 105 runs. The Fermi wavelengths correspond to Fermi energies between $0.07t$ and $0.37t$

Note that the λ_F-scale of figure 4.5 is different than that of figure 4.4. This is because the system size grows with the Fermi wavelength, and taking larger values would take tremendous amounts of computation time. This calculation has been done multiple times for less than 14 modes to fasten it up, but the results was no different from this figure: the variance still increases with the Fermi wavelength. From this figure, it it is seen even easier that the increase in variance is cubically proportional to the increase in wavelength. Another thing to notice is the coinciding peaks in the orange $E_F - 0.03t$-line around $\lambda_F \approx 57a$. This strongly suggests that the two figures follow the exact same trend of increasing, and share eventual numerical deviations. It also suggests that this phenomenon of increasing diffusivity with increasing wavelength is not dependent on the system size at all. That means that reverse law of reflection must be solely dependent on the Fermi wavelength and the distance to the disorder mean. To visualise what is happening, once again the density of states is shown for the relevant parameters in figure 4.6.

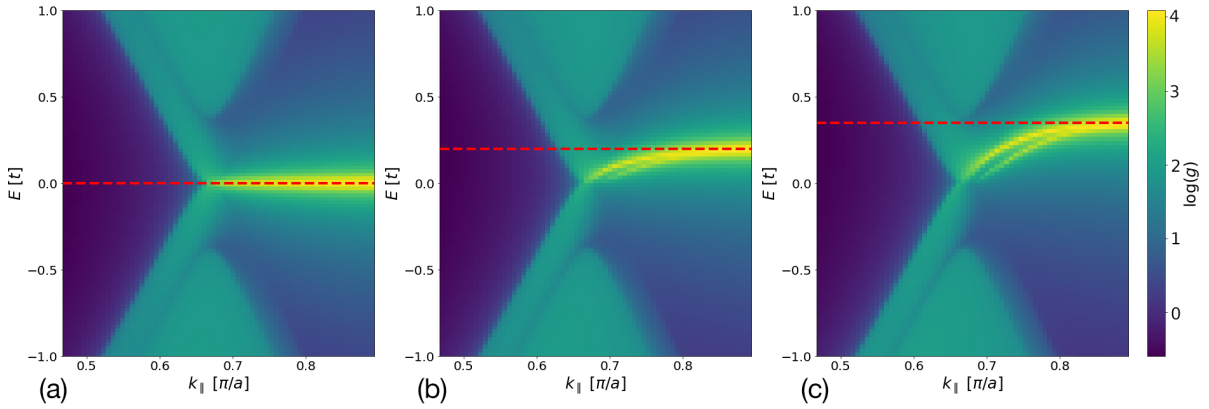

Figure 4.6: Local density of states at the edge of a semi-infinite zigzag edged bilayer graphene sheet. Used parameters were $L = 240a$ and $s_d = 0.035t$. The dotted lines indicate the value of mean disorder used for the images, being $V_d = 0$ for (a), $V_d = 0.2t$ for (b), and $V_d = 0.35t$ for (c). These three figures were made using Kwant [10].

An explanation of this law-of-reflection-rejecting behaviour is made here, first for the blue lines in figure 4.4 and 4.5. For that line it holds that $E_F = V_d$, and that the variance increases with increasing Fermi wavelength, i.e. decreasing energy. Looking at figure 4.6 and acknowledging that the dotted lines indicate both the Fermi energy and disorder mean, it means that the diffusivity increases in order of (c), (b), (a). The right side of the parabolas are missing a bit, and therefore the overlap indeed seems to increase as the energy lowers. As this comparison is merely based on the conclusions of the paper about graphene, read this discussion with a critical view. The phenomenon of a breakdown of the law of reflection thus still appears, though a specific reason for being increasing in variance instead of constant has not been found. The case of the green line in figure 4.4 and 4.5 is now even more peculiar.

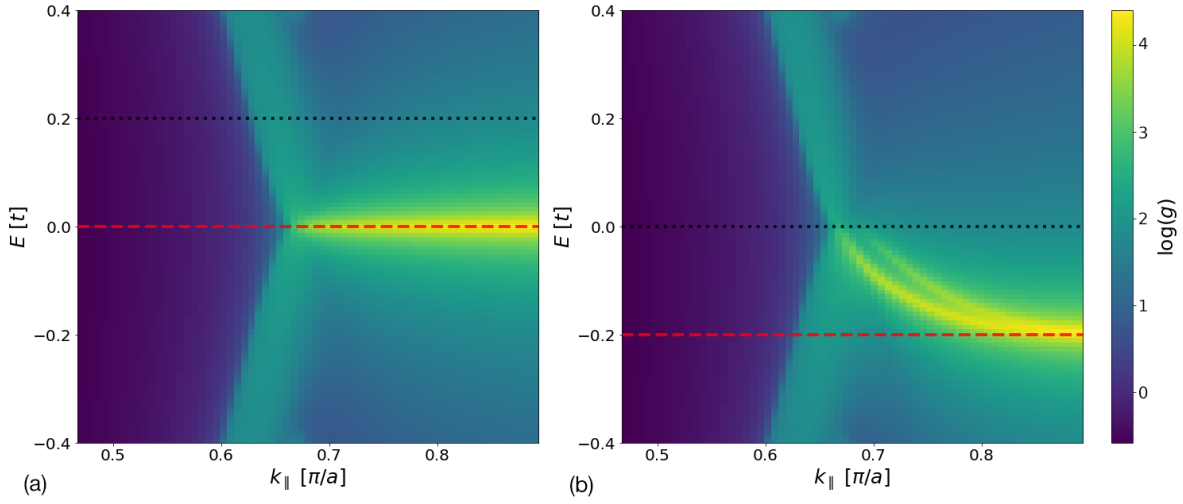

Figure 4.7: Local density of states at the edge of a semi-infinite zigzag edged bilayer graphene sheet. Used parameters were $L = 240a$ and $s_d = 0.035t$. The red lines indicate the value of mean disorder used for the images, and the black dots are the Fermi energy. These values are $V_d = 0$ and $E_F = 0.2t$ for (a), and $V_d = -0.2t$ and $E_F = 0$ (b). These two figures were made using Kwant [10].

For those green lines, the value of mean disorder was $V_d = E_F - 0.2t$. Two cases are depicted in figure 4.7 for different Fermi energies. The numerical simulations show that reflections at the scenario shown in (b) are more diffusive than the ones in (a). The same reasoning could be used as for the previous case, but now no actual overlap is present with the edge band. Only a dimmed part of the band is still present at the Fermi energy in both cases, which is slightly higher than in monolayer graphene. The increasing narrowness of the parabola for lower energies might let the remnant of the edge band somehow dominate, causing the variance of the scattering angle to keep increasing. This is just speculative guessing however, and more research is needed to find the root of this phenomenon. As mentioned, the trends of scattering angle variance versus Fermi wavelength and scattering phase versus boundary periodicity were thought to be the same, and thus the phase will be computed numerically as well in the next section.

4.3. Variance of the scattering phase

To numerically find the scattering phase, a system with a Fermi energy of zero is preferred. This is not possible in Kwant, as it normalises the modes using the particle current operator J, just as in chapter 3. The parabolic form of the dispersion at low energies causes the Fermi velocity of those electrons to also converge to zero, and thus an error is returned by Kwant. This problem is avoided by using very small Fermi energies, but still finite. This has been done in the following figure, where a value of $E_F = 10^{-5}\,t$ was chosen. This energy corresponds to a Fermi wavelength of over thirty times the maximum system length of $L = 300$, which should be large enough to approximate a zero energy scenario.

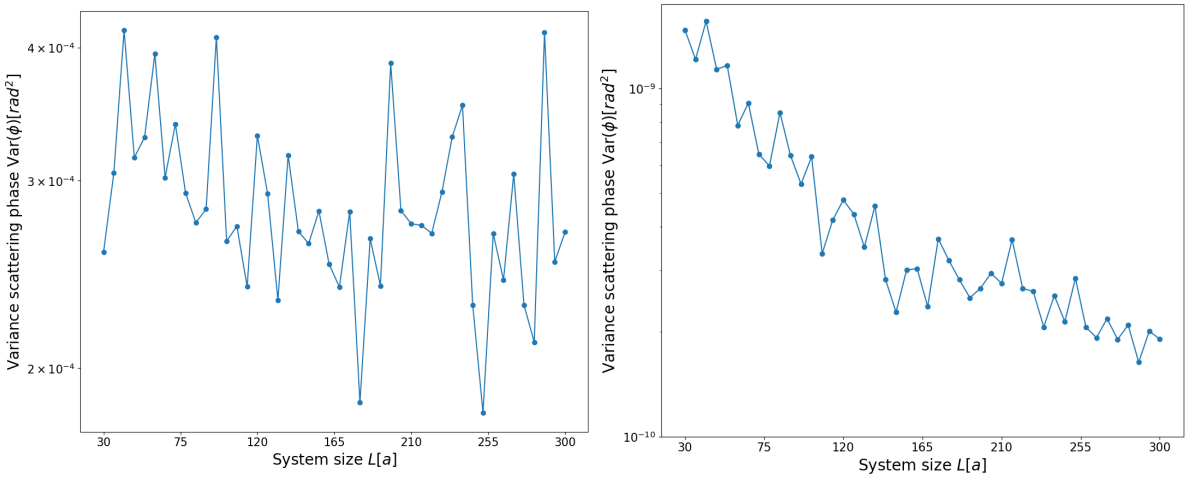

(a) (b)

Figure 4.8: Variance of the scattering phase for different boundary periodicity constants. Left figure has a disorder mean of $V_d = 0$, right one of $V_d = 0.2t$. Both figures have a Fermi energy of $E_F = 10^{-5}\,t$, a disorder strength of $s_d = 0.035t$ and are averaged over 100 runs.

These numerical simulations confirm the results of the tight binding analysis done in the previous chapter. Indeed, the scattering phase remains constant when the flat edge band overlaps with the Fermi energy, but decreases as $1/L$ when it doesn't. One thing to note here is the scale of the vertical axis. In graphene, the variances found were a tad higher, deviating with a factor of 10 with the variance of the scattering angle. Nonetheless, only the trends were analysed in chapter 3, and therefore it still confirms the findings. This actually means that in bilayer graphene systems with a zigzag edge, the variance of the scattering angle versus the Fermi wavelength and the variance of the scattering phase versus the boundary periodicity do not coincide.

To check that using a small but finite Fermi energy is a reliable way to describe zero-energy systems, the structure of the scattering matrix was looked at. First a large set of scattering matrices was computed, in the regime of $10^{-12} \leq E_F \leq 10^{-1}$ and for multiple disorder configurations. Then for each of those energies E, the average of the scattering matrix over the disorder configurations was taken: $S_{avg,E}$. A unitary matrix of this averaged scattering matrix is made, so that all the original matrices can be multiplied with it, ensuring that they are unitary as well. To do this, a *singular value decomposition*[23] is used, such that:

$$S_{avg,E} = U\Sigma V^\dagger \tag{4.2}$$

Here Σ contains the singular values of $S_{avg,E}$ on its diagonal, and U and V are unitary. The singular value matrix Σ is thrown away to keep just the unitary part, and the new unitary average scattering matrix is made as $S_{U,E} = UV_h$. After that, every original matrix is multiplied from the left with this new matrix, so the resulting matrix is unitary as well. Lastly, the matrix logarithm is used on these matrices, resulting in a skew-hermitian matrix. This is because every unitary matrix U can be written as $U = e^{iH}$, where H is hermitian. The variance of the elements of these hermitian matrices is shown in figure 4.9 below.

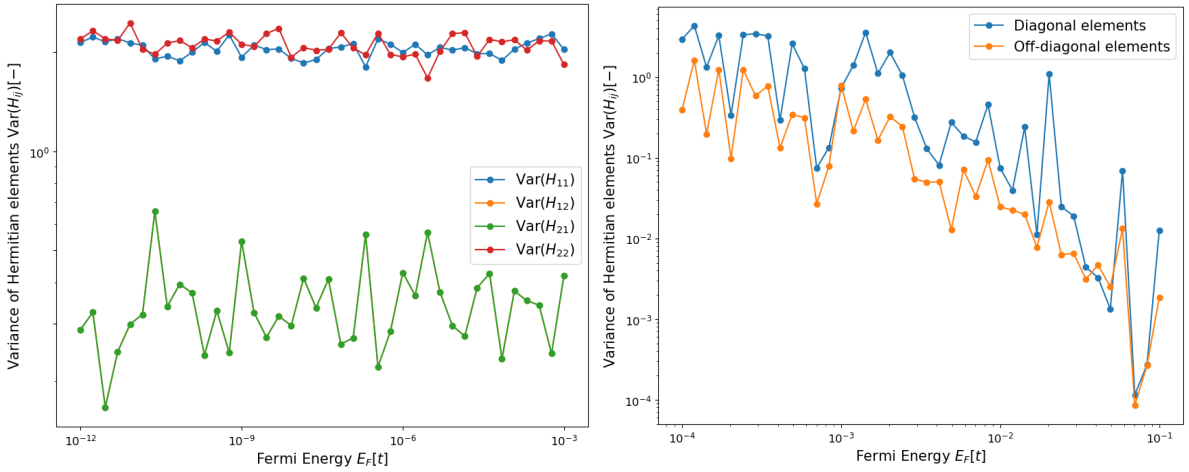

(a) (b)

Figure 4.9: Variance of the elements of the hermitian generators of the unitarised scattering matrices, for different Fermi energies. Both figures have a system size of $L = 240a$, and a disorder strength of $s_d = 0.01\,t$, and are averaged over 200 runs.

Figure 4.9a confirms that the variances of the 2×2 hermitian matrix elements do not change when the Fermi wavelength becomes larger than the system size, which is when the energy goes slightly below 10^{-2} according to equation 2.7. This means that these low energies may be used interchangeably, as they would produce the same results. In figure 4.9b however different lines are depicted: the variance of the diagonal elements and the off-diagonal elements. This is because the scattering matrices for the energy scale of this figure differ in size, due to a different number of allowed modes. Therefore this visualisation was chosen, to show that the limit $E_F \to 0$ is indeed stable and may be used reliably.

The current findings summarised are that the variance of the scattering angle increases with the Fermi wavelength, and that the variance of the scattering phase versus the system periodicity does not share the same pattern. To analyse this even further, two systems similar to bilayer graphene, yet simpler were considered.

4.4. Simpler systems

To narrow the problem down of this law of reflection-rejecting behaviour, two other systems were looked at. The first of those is a simple square lattice, which also has a parabolic dispersion. Details of this system can be found in appendix A, including the tight binding model and the density of states. One key difference with bilayer graphene, is that a simple square lattice does not have edge bands. This means that the reasoning used previously for overlapping is not applicable here, and therefore no odd behaviour is expected.

Figure 4.10 was made depicting the variance of the scattering angle for different distances to the disorder mean, akin to figure 4.4. As hypothesised, this system neatly abides the law of reflection: the larger the wavelength of the electrons, the smaller the variance of the scattering angle, so reflections are more specular. The Fermi wavelength scale only goes to $\lambda_F = 45a$, as it already reaches a numerical zero at higher values. This is expected as well, as electrons with big wavelengths shouldn't reflect diffusively. At least, that was thought to be the case.

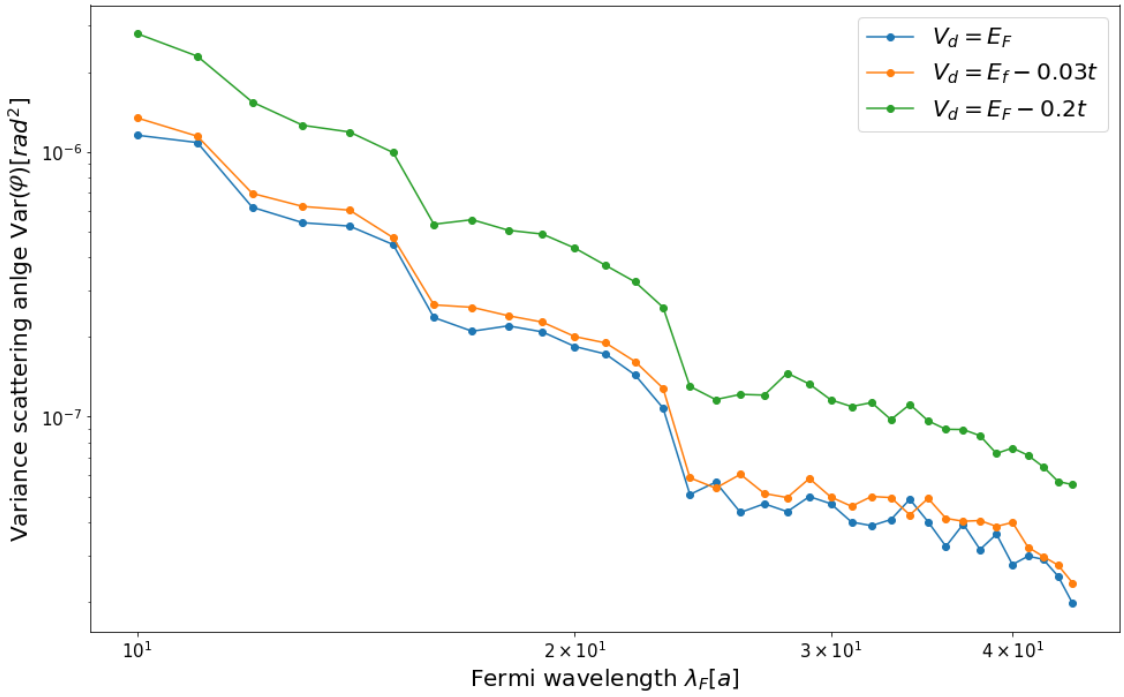

Figure 4.10: Variance of the scattering angle versus the Fermi wavelength in a simple square system. Parameters used are a system size of $L = 300a$, $s_d = 0.05t$, and it is averaged over 105 runs.

Another way to analyse this problem is by looking at *split* bilayer graphene, where the two layers are disconnected. This should result in electronic behaviour as found in graphene. Disconnecting the two layers in the tight-binding model can either be done by removing the hopping altogether, or by giving it a very large value. The values used for hoppings before as in [7] were $\gamma_0 = 3.16t$ and $\gamma_1 = 0.381t$, where the second was the interlayer hopping. In the following figures, this value was raised to $\gamma_1 = 5t$ which should simulate disconnected layers. First of all, in figure 4.11 the density of states for a system disconnected in this manner is depicted.

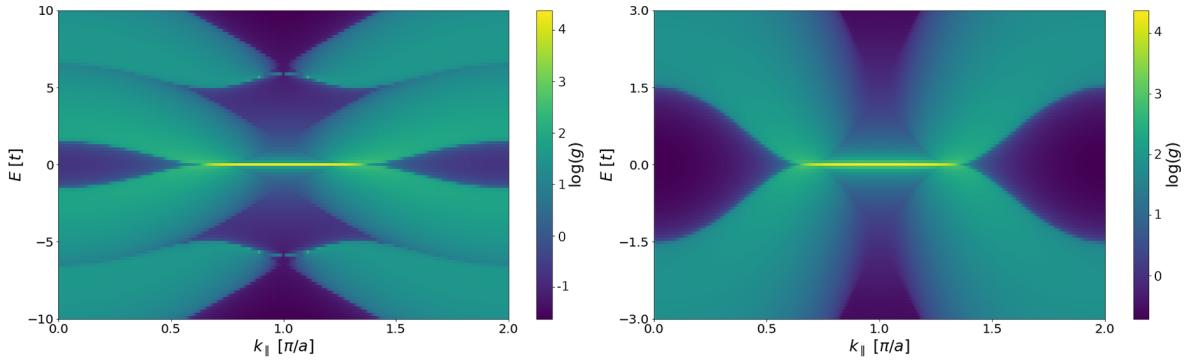

(a) (b)

Figure 4.11: Density of states for a bilayer graphene system where the interlayer hopping is set to $\gamma_1 = 5t$. Figure (a) shows the entire first Brillouin zone, and (b) is zoomed in to the two K-points. The system used to generate this had a size of $L = 300a$, and a disorder strength of $s_d = 0.035t$. Figure made using Kwant [10].

There are two major changes to the density of states, compared to the connected bilayer system. The first one is that two outer parabolas shifted away from zero: the distance of the bottom of the upper parabola and the top of the bottom parabola to the K-points is actually exactly γ_1. This is clearly seen in figure 4.11a. The other one is the steepness of the parabola, especially when compared to the connected density of states in figure 2.7d. This can easily be explained by the fact that the relation between the energy and the wavelength is also dependent on the changed hopping parameter γ_1, as seen in equation 2.7.

Now the question is what happens with the specularity of the reflections. In the next figure the variance can once again be seen for this system for different distances between the Fermi energy and the disorder mean.

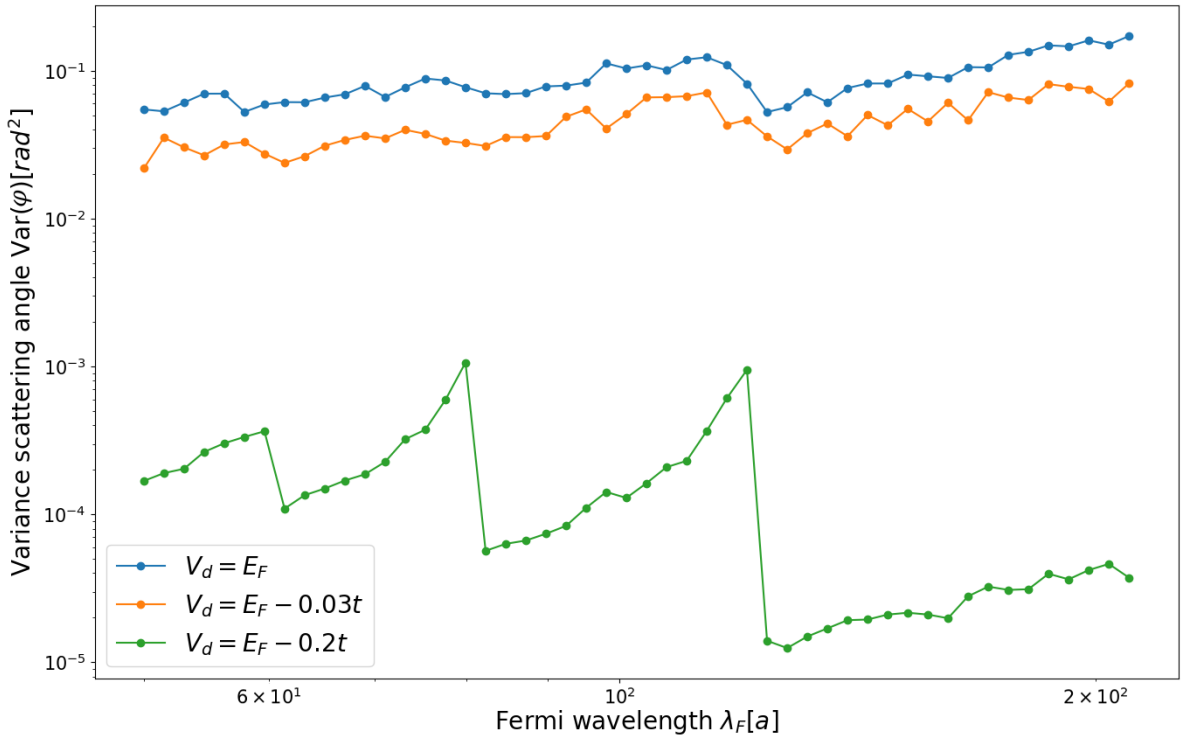

Figure 4.12: Variance of the scattering angle versus the Fermi wavelength for a system with interlayer hopping of $\gamma_1 = 5t$. Parameters used are a system size of $L = 240a$, $s_d = 0.035t$, and it is averaged over 105 runs. The Fermi wavelengths correspond to energies between $0.003t$ and $0.024t$.

This figure is also heavily discontinuous in the bottom line. This is also due to the just mentioned fact that the relation between the energy and the wavelength is also dependent on the changed hopping parameter γ_1. While the range of Fermi wavelengths doesn't change in comparison to figure 4.4, the regime of energy the variance is calculated for shrinks down to $0.003t \leq E_F \leq 0.024t$. The amount of modes thereby shrinks more noticeably, as lower energies allow fewer distinct modes.

What is great about this figure is the generally decreasing trend of the bottom line, and the roughly constant value of the upper two. This means that the split bilayer graphene system copies the behaviour of graphene, where the same trends of variance are found. In the bottom line, there is a small tendency of rising between the discontinuities. This is the consequence of the overlap between the edge band and the Fermi energy being easier, as the parabolas are a lot steeper, as seen in figure 4.11b.

Before this chapter ends, a note about the experimental detection of this phenomenon will be made. In the original graphene paper, a magnetic focusing device was proposed. This plan used a system composed of a big plane of bilayer graphene, with two parallel lead attached. Between those leads, a zigzag edge is put. By applying a magnetic field perpendicular to the plane, electrons inserted from one of the leads would bend their trajectories towards the zigzag boundary. When scattered off of this edge, the magnetic field would bend their trajectories again and the electrons end up in the other lead in an ideal scenario. By tuning the voltage on the zigzag edge, the Fermi energies of the electrons and the strength of the magnetic field, at a certain point a conductance dip is found: this is where the reflections suddenly become diffusive. The same experiment could be used to measure this effect in bilayer graphene, but the original plan took a lot of trial and error of finding the perfect parameters. Therefore another experiment might be better to measure this effect.

This wraps up the numerical findings of this works, which show an even bigger breakdown of the law

of reflection. Essentially, reflections within bilayer graphene systems behave oppositely to those on regular mirrors. The final concluding remarks and suggestions for future research are found in the next and final chapter.

5

Conclusion

Using a tight-binding model, it was found that diffusivity of electron scattering on zigzag edges in bilayer graphene systems increase with the wavelength. This happens regardless of the distance between the Fermi energy and disorder mean on the outermost atoms, as long as their is some disorder. The increasing diffusivity was shown with a numerical simulation in Kwant [10], in which the variance of the scattering angle was calculated for different parameters. The trend of increasing variance was finally narrowed down to only being related to the Fermi wavelength in a cubical manner.

Further numerical calculations showed that the variance of the scattering phase remained to seem constant or decrease, in similar regimes as found in graphene. These calculations have been backed up with a symbolical derivation of the scattering matrix using the tight-binding model. This is as surprising as the other result, as it was previously thought that there was a connection between the trends of $\mathrm{Var}(\varphi)$ vs λ and $\mathrm{Var}(\phi)$ vs L. This does not seem to hold here, and as this claim never had any real physical backup it can't be taken for granted anymore.

This counter-intuitive behaviour is supported by the presence of edge states, which can be found by looking at the density of states. The parabolic nature of dispersion around the K-points in bilayer graphene suggests an increase of overlap with the edge states as the Fermi energy decreases. Since the Fermi energy is inversely proportional to the Fermi wavelength, a higher overlap is found for higher wavelength, and thus more diffusivity.

To validify this result even more, one could research the boundary conditions for a single-valley bilayer graphene edge Hamiltonian. With this a derivation of the scattering phase using the continuum model can be made, which would support the findings of this work. Another interesting research would be studying the scattering angles in Weyl semimetals. This material has edge states as well, connecting two parabolic bands in three dimensional density of states.

List of references

[1] A. Einstein and L. Infeld. The evolution of physics: The growth of ideas from early concepts to relativity and quanta. Cambridge University Press, 1938.

[2] E. Walter, T. Ö. Rosdahl, A. R. Akhmerov, and F. Hassler. Breakdown of the law of reflection at a disordered graphene edge. Phys. Rev. Lett. 121, 136803, 2018.

[3] Y.-W. Son, M. L. Cohen, and S. G. Louie. Energy gaps in graphene nanoribbons. Phys. Rev. Lett. 97, 216803, 2006.

[4] D. Halbertal, M. Ben Shalom, A. Uri, K. Bagani, A. Y. Meltzer, I. Marcus, Y. Myasoedov, J. Birkbeck, L. S. Levitov, A. K. Geim, and E. Zeldov. Imaging resonant dissipation from individual atomic defects in graphene. Science 08 Dec 2017: Vol. 358, Issue 6368, 2017.

[5] X. Song, J. Hu, and H. Zeng. Two-dimensional semiconductors: recent progress and future perspectives. Journal of Materials Chemistry C. 1 (17): 2952, 2013.

[6] MarvinSketch (version 19.10). Developed by chemaxon. http://www.chemaxon.com/products/marvin/marvinsketch/, 2019. Used: 2019-05-09.

[7] E. McCann and M. Koshino. The electronic properties of bilayer graphene. Rep. Prog. Phys. 76, 056503, 2012.

[8] A.R. Akhmerov and C.W.J. Beenakker. Boundary conditions for dirac fermions on a terminated honeycomb lattice. Phys. Rev. B 77, 085423, 2008.

[9] A.R. Akhmerov. Dirac and majorana edge states in graphene and topological superconductors. Institute Lorentz, Faculty of Science, Leiden University, 2011.

[10] C. W. Groth, M. Wimmer, A. R. Akhmerov, and X Waintal. Kwant: a software package for quantum transport. New J. Phys. 16, 063065, 2014.

[11] H. Johnston. Weyl fermions are spotted at long last. Physics World, July 23rd 2016, 2016.

[12] S. Datta. Electronic transport in mesoscopic systems. Cambridge University Press, 2013.

[13] D.J. Griffiths. Introduction to quantum mechanics (2nd edition). Prentice Hall, ISBN 978-0-13-111892-8, 2004.

[14] F. Bloch. Über die quantenmechanik der elektronen in kristallgittern. Zeitschrift für Physik (7-8), Volume 52, 1928.

[15] Wolfram Research Inc. Mathematica (version 12.0). Champaign, Illinois, 2019.

[16] E.O. Brigham. The fast fourier transform and its applications. Englewood Cliffs, N.J.: Prentice Hall, 1988.

[17] R.A. Horn and C.R. Johnson. Topics in matrix analysis. Cambridge University Press, 1991.

[18] Wikipedia. Block matrix inversion. https://en.wikipedia.org/wiki/Block_matrix#Block_matrix_inversion, 2019. Visited: 2019-07-04.

[19] F. Zhang. The schur complement and its applications. Springer. doi:10.1007/b105056, 2004.

[20] P. Bachman. Die analytische zahlentheorie. 2. Leipzig: Teubner., 1894.

[21] M.V. Berry and R.J. Mondragon. Neutrino billiards: time-reversal symmetry-breaking without magnetic fields. 412. Proc. R. Soc. Lond. A, 1987.

[22] W. Pauli. Principles of wave mechanics. handbuch der physik. 24. Berlin: Springer. p. 162, 1933.

[23] S. Banerjee and A. Roy. Linear algebra and matrix analysis for statistics, texts in statistical science (1st ed.). Chapman and Hall/CRC, ISBN 978-1420095388, 2014.

Appendix A: Simple square lattice

The simple square lattice has the following Bravais lattice vectors and atom coordinates:

$$\mathbf{a}_1 = (a,0), \quad \mathbf{a}_2 = (0,a), \quad \mathbf{s}_1 = (0,0) \tag{5.1}$$

As the lattice vectors are already orthogonal, no supercell has to be constructed. A wavefunction can thus already be made in the same fashion as the bilayer graphene model:

$$\psi = \begin{pmatrix} \psi_L \\ \psi_B \end{pmatrix} = \begin{pmatrix} \vdots \\ \psi_L(2) \\ \psi_L(1) \\ \psi_B \end{pmatrix} = \begin{pmatrix} \vdots \\ \psi_L(2,0) \\ \psi_L(1,L-1) \\ \vdots \\ \psi_L(1,0) \\ \psi_B(L-1) \\ \vdots \\ \psi_B(0) \end{pmatrix} \tag{5.2}$$

Note that the wavefunctions here now only contains information of the amplitude on one single atom. The onsite energy of all atoms is set to $E_0 = 2t$, and the hopping energies to $T_{x/y} = -t$, to ensure that the parabolic dispersion starts in the origin of the reciprocal space. Now the lead Hamiltonian and lead translation matrix look like:

$$H_L = \begin{bmatrix} 2t & -t & & -t \\ -t & 2t & \ddots & \\ & \ddots & \ddots & -t \\ -t & & -t & 2t \end{bmatrix}, \quad T_L = \begin{bmatrix} -t & & & \\ & -t & & \\ & & \ddots & \\ & & & -t \end{bmatrix} \tag{5.3}$$

To distort the boundary, once again random onsite potentials are added on top off the onsite energy of $2t$, resulting in the boundary Hamiltonian:

$$H_B = \begin{bmatrix} 2t+V_0 & -t & & -t \\ -t & 2t+V_1 & \ddots & \\ & \ddots & \ddots & -t \\ -t & & -t & 2t+V_{N-1} \end{bmatrix}, \quad T_{LB} = T_L \tag{5.4}$$

The translation from the lead to the boundary is the same as the translation into the lead as the lead cells and boundary cells contain the same amount of atoms, which is one. The complete tight binding Hamiltonian is now, using that $T_L = T_L^\dagger$:

$$H = \begin{bmatrix} \ddots & \ddots & & \\ \ddots & H_L & T_L & \\ & T_L & H_L & T_L \\ & & T_L & H_B \end{bmatrix} \tag{5.5}$$

The density of states can now be computed by Kwant. It is indeed parabolic, and no edge states appear between the bottoms of the parabolas:

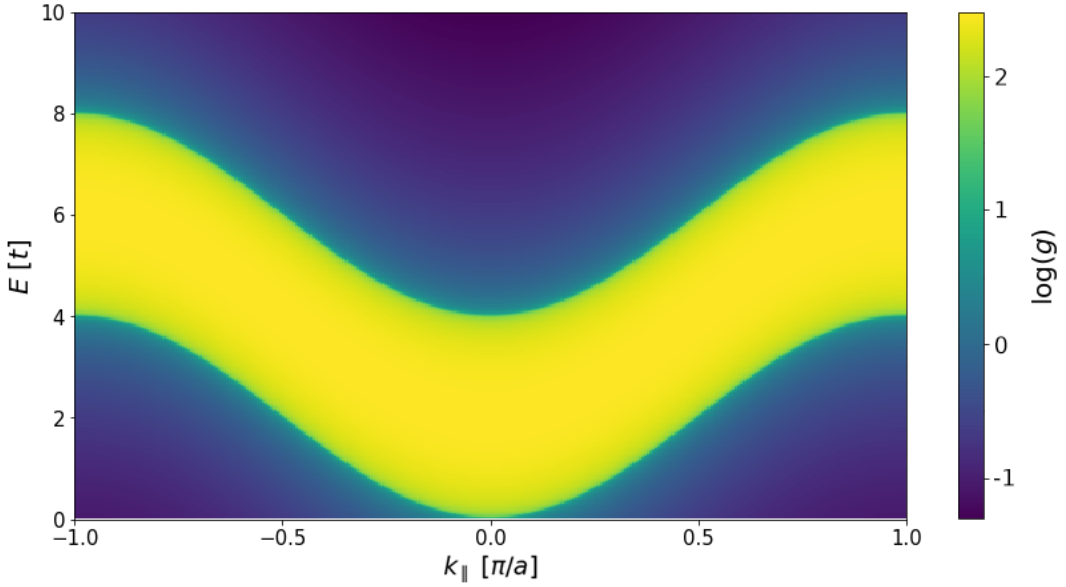

Figure 5.1: Density of states of a simple square lattice. The used parameters are $L = 300a$, and this figure was made in Kwant [10].

One last thing to verify the parabolic nature, is once again showing the allowed momenta at a certain energy with their velocities, just like in figure 3.2:

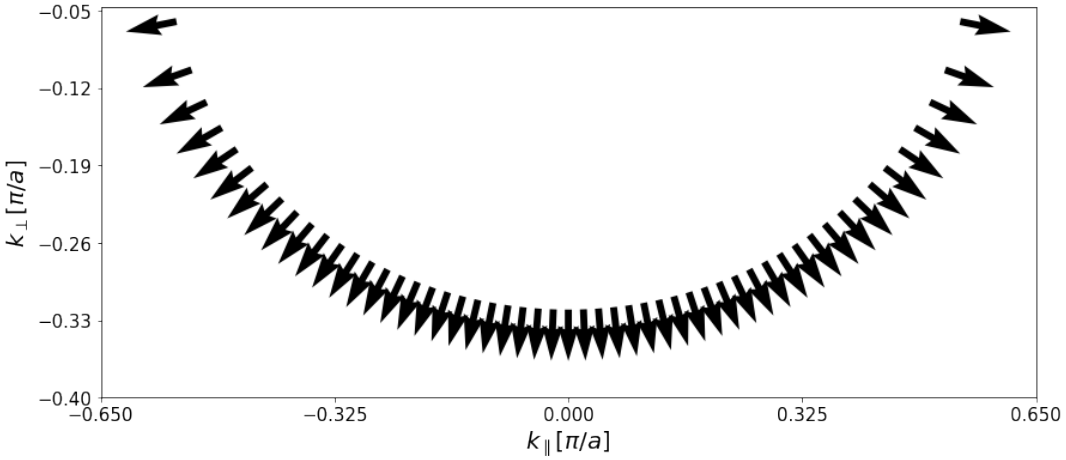

Figure 5.2: Allowed momenta in a simple square lattice. Used parameters are $L = 300a$ and $E_F = 0.3t$, and the arrows indicate the velocities corresponding to those momenta.